

Infrared Diagnostics for the Extended 12 μm Sample of Seyferts

Stefi A. Baum¹, Jack F. Gallimore², Christopher P. O’Dea³, Catherine L. Buchanan⁴,
Jacob Noel-Storr¹, David J. Axon³, Andy Robinson³, Moshe Elitzur⁵, Meghan Dorn^{1,6},
Shawn Staudaher¹, Martin Elvis⁷

ABSTRACT

We present an analysis of Spitzer IRS spectroscopy of 83 active galaxies from the extended 12 μm sample. We find rank correlations between several tracers of star formation which suggest that (1) the PAH feature is a reliable tracer of star formation, (2) there is a significant contribution to the heating of the cool dust by stars, (3) the H₂ emission is also primarily excited by star formation.

The 55-90 vs. 20-30 spectral index plot is also a diagnostic of the relative contribution of Starburst to AGN. We see there is a large change in spectral index across the sample: $\Delta\alpha \sim 3$ for both indices. Thus, the contribution to the IR spectrum from the AGN and starburst components can be comparable in magnitude but the relative contribution also varies widely across the sample.

We find rank correlations between several AGN tracers. We find correlations of the ratios [OIII] λ 5007/[OIV]26 μm and [OIII] λ 5007/[NeV]14 μm with the Sil strength which we adopt as an orientation indicator. This suggests that some of the [OIII] λ 5007 emission in these Seyferts is subject to orientation dependent obscuration as found by Haas et al. (2005) for radio galaxies and quasars. There is no correlation of [NeV] EW with the Sil 10 μm strength indicating that the [NeV] emission is not strongly orientation dependent. This suggests that the

¹Chester F. Carlson Center for Imaging Science, Rochester Institute of Technology, 54 Lomb Memorial Drive, Rochester, NY 14623

²Department of Physics and Astronomy, Bucknell University, Lewisburg, PA 17837; Currently visiting NRAO, 520 Edgemont Rd., Charlottesville, VA 22903

³Department of Physics, Rochester Institute of Technology, 84 Lomb Memorial Drive, Rochester, NY 14623

⁴School of Physics, University of Melbourne, Parkville, Victoria, 3010 Australia

⁵Department of Physics and Astronomy, University of Kentucky, Lexington, KY 40506

⁶Rush-Henrietta High School, 1799 Lehigh Station Rd., Henrietta, NY 14467

⁷Harvard-Smithsonian Center for Astrophysics, 60 Garden Street, Cambridge, MA 02138

obscuring material (e.g., torus) is not very optically thick at $14\mu\text{m}$ consistent with the results of Buchanan et al. (2006).

We search for correlations between AGN and Starburst tracers and we conclude that the AGN and Starburst tracers are not correlated. This is consistent with our conclusion that the relative strength of the AGN and Starburst components varies widely across the sample. Thus, there is no simple link between AGN fueling and Black Hole Growth and star formation in these galaxies.

The density diagnostic [NeV] $14/24\ \mu\text{m}$ and [SIII] $18/33\ \mu\text{m}$ line ratios are consistent with the gas being near the low density limit, i.e., $\sim 10^3\ \text{cm}^{-3}$ for [NeV] and $n_e \sim \text{few hundred cm}^{-3}$ for [SIII].

The distribution of Sil $10\ \mu\text{m}$ and $18\ \mu\text{m}$ strengths is consistent with the clumpy torus models of Sirocky et al. (2008).

We find a rank correlation between the [NeV] $14\mu\text{m}$ line and the $6.7\ \mu\text{m}$ continuum which may be due to an extended component of hot dust.

The Sy 2's with a Hidden Broad Line Region (HBLR) have a higher ratio of AGN to Starburst contribution to the SED than Sy 2's without an HBLR. This may contribute to the detection of the HBLR in polarized light. The Sy 2's with an HBLR are more similar to the Sy 1's than they are to the Sy 2's without an HBLR.

Subject headings: galaxies: active - galaxies: Seyfert - galaxies: spiral - infrared: galaxies

1. Introduction

The basic paradigm for nuclear activity in galaxies, an accretion disc around a super massive black hole (SMBH), is well-established. However, we have at best a sketchy understanding of how SMBH are formed and what role nuclear activity plays in galaxy evolution. As we learn more about the formation and evolution of normal galaxies, and better understand the physics of active galactic nuclei (AGNs), it is becoming clear that these processes are intimately connected. The ubiquity of super massive black holes and the observed relation between black hole mass and bulge mass (Merritt & Ferrarese 2001; Gebhardt et al. 2000) suggest that nuclear activity may be closely connected to star formation in all galaxies. Accretion onto a black hole, which powers AGNs, requires available fuel in the nuclear region. Gas infall is also likely to be associated with bursts of star formation (Hernquist & Mihos 1995; Mihos & Hernquist 1996). Furthermore, AGNs deposit energy in the surrounding interstellar medium (ISM) via ionizing radiation, radio jets and perhaps winds, possibly

triggering star formation. Circumnuclear star formation has been observed in AGN and a link between nuclear activity and star formation is also supported by a recent finding that the mean stellar age of narrow-line AGNs is much younger than in similar normal spiral galaxies (Kauffmann et al. 2003). However, the interaction between active nuclei and their host galaxies remains poorly understood.

The mid-IR includes important diagnostics such as the PAHs, Sil features, and fine structure lines (Spinoglio & Malkan 1992; Voit 1992b; Genzel et al. 1998; Laurent et al. 2000). Previous mid-IR spectroscopic studies of AGN have shown that these diagnostics allow separation of AGN and starburst properties, as well as provide constraints on orientation and obscuration of the central torus (Genzel et al. 1998; Laurent et al. 2000; Clavel et al. 2000; Sturm et al. 2002; Haas et al. 2005; Weedman et al. 2005; Ogle et al. 2006; Shi et al. 2006; Hao et al. 2007; Spoon et al. 2007).

This paper is part of a series on a Spitzer study of the Extended $12\mu\text{m}$ Sample of Seyfert galaxies. Buchanan et al. (2006) presented low resolution IRS spectra of the first 51 (of 83) sources and demonstrated the variety of mid-IR spectral shapes due to the relative mix of comparable contributions from starburst and AGN. They examined the ratio of IR to nuclear radio flux density and showed that the ratio is a factor of two larger in Sy 1's than Sy 2's between 15 and 35 μm suggesting the torus emission is anisotropic by a factor of two at these wavelengths. Additional preliminary results have been presented by Buchanan et al. (2008). Other papers currently planned in the series will present (1) an atlas of all the data (Gallimore et al. 2009a), (2) models of the mid- to far- IR SEDs which combine both starburst and AGN contributions (Gallimore et al. 2009b), and (3) UKIRT observations of the near-IR emission and discuss constraints on the relative mix of starburst and AGN contributions to the spectrum (Buchanan et al. 2009). In this paper we examine diagnostic features (PAH, Sil, fine structure lines, H_2 , continuum slope) in the IRS spectra and discuss the implications for the AGN-Starburst connection and obscuration of the central engine. We note that independent groups have also published results based on our data. Maiolino et al. (2007) used observations of some Sy 1's from Buchanan et al. (2006) as a comparison sample for their study of high luminosity QSOs. Deo et al. (2007) obtained low resolution Spitzer IRS observations of 12 Sy 1.8 and 1.9 and combined the results with archival data of 57 Sy 1's and Sy 2's from Buchanan et al. (2006) and Weedman et al. (2005). High resolution IRS observations of a subsample of 29 sources are presented by Tommasin et al. (2008). Recently Wu et al. (2009) published a study of 103 Seyferts which included our IRS data. Gallimore et al. (2009a) show that there are systematic differences between our values for the PAH and Sil features and those of Wu et al. (2009) which are due to the different analysis techniques used (PAHFIT vs. Spline-fitting). Nevertheless, we agree on the overall trends which are common to both papers.

2. Spitzer Observations

2.1. The Sample of AGN

The properties of the sample are discussed by Buchanan et al. (2006) and Gallimore et al. (2009a). The sample comprises all galaxies identified as Seyferts or LINERS from the extended 12 μm sample of Rush et al. (1993) that have $cz < 10000 \text{ km s}^{-1}$. The potential advantage of the 12 μm sample is its perceived resistance to wavelength-dependent selection effects (Spinoglio & Malkan 1989). Note that there may in fact be selection effects in the sample due to anisotropic emission from the torus at 12 μm (Buchanan et al. 2006). The redshift criterion was included to ensure that the smallest possible physical size was probed by the fixed Spitzer apertures in order to better exclude host galaxy emission. The data include IRAC imaging, IRS spectral mapping, and MIPS SED spectra as described by Gallimore et al. (2009a).

The spectral classifications were obtained by a thorough search of the literature for each galaxy; see Table 1 of Gallimore et al. (2009a). For the purposes of comparing the Seyfert types we consider Seyfert types 1.*n* (i.e. types 1.0, 1.2, 1.5, 1.8, and 1.9 as well as narrow line Seyfert 1's) to be Sy 1's, and objects with no broad permitted lines to be Sy 2's. We consider the properties of the Seyferts with hidden broad line regions (HBLRs) separately and compare them to the Sy 1's and Sy 2's. We refer to the sum of the Sy 1's, Sy 2's, and hidden Sy 1's as the combined sample. The resulting sample contains 83 sources of which 7 are now classified as HII galaxies, 6 are LINERS and the remaining 70 are Seyferts (27 Sy 1-1.5, 17 Sy 2 with HBLR, 20 Sy 2 without HBLR, and 6 Sy 1.8-1.9). The sample is listed in Table 1 of Gallimore et al. (2009a).

2.2. IRS Observations and Data Reduction

The sample galaxies were observed by Spitzer IRS (Houck et al. 2004) in spectral mapping mode, using the Short-Low and Long-Low modules. The modules cover a wavelength range of $\sim 5 - 36 \mu\text{m}$, with a resolving power ($\lambda/\Delta\lambda$) ranging from 64 to 128. The integration times were 6 seconds per slit pointing. Details of the observing and reduction are given by Gallimore et al. (2009a) and are summarized here.

The spectral maps were constructed to span $> 10''$ in the cross-slit direction and centered on the target source. The observations were stepped perpendicular to the slit by half slit-width spacings. For the SL data, the mapping involved 13 observations stepped by $1.8''$ perpendicular to the slit, and for the LL data, 5 observations stepped by $5.25''$ perpendicular

to the slit. The resulting spectral cubes span roughly $25.3'' \times 54.6''$ ($5.3 - 14.2 \mu\text{m}$) for the SL data and $29.1'' \times 151''$ ($14.2 - 36 \mu\text{m}$) for the LL data.

The raw data were processed through the Spitzer BCG pipeline, version S15.3.0. Sky subtraction employed off-source orders. In SL and LL observations, the source is centered in first or second order separately, with the “off-order” observing the sky at an offset position along the slit orientation. Sky frames were constructed using median combinations of the off-source data and subtracted from the on-source data of matching order. No detectable contamination appeared in the sky frame images.

Data cubes were constructed and edited for cosmic-rays and spurious pixels using the CUBISM software package developed by the SINGS IRS team (Smith et al. 2007b). We used synthetic, $20''$ diameter circular apertures to extract the spectra.

To calibrate the flux scale, we employed archival IRS staring and spectral mapping observations of the calibrator stars HR7341 (SL) and HR6606 (LL). The staring mode spectra were extracted using SPICE (Spitzer Science Center 2006), and the spectral mapping observations were processed as described above. The flux calibration curve was determined by the ratio of the flux-calibrated staring mode spectra to the uncalibrated cube-extracted spectra. This flux calibration was applied to all target sources observed in spectral mapping mode. Based on inspection of the spectral overlaps between modules and orders the calibration is self-consistent to within 5% across the IRS spectrum. The only exception was NGC 4151, SL order 1, which had to be scaled down by $\sim 15\%$ to match the neighboring SL order 2 and LL order 2 spectra, perhaps owing to a residual pipeline error. After applying a uniform scaling to SL order 1, the spectrum matched well the neighboring spectral overlaps.

Archival data of our sample, such as obtained by the SINGS collaboration, were processed in the same manner. There are however a few sources for which only staring mode observations are available for the SL module: NGC 526A, NGC 3227, NGC 4941, IC 5063, NGC 7172, and NGC 7314. The staring mode spectra were extracted using SPICE and scaled to match IRAC 5.8 and $8.0 \mu\text{m}$ photometry obtained as part of this project (Gallimore et al. 2009a).

2.3. MIPS-SED Observations and Data Reduction

The sample galaxies were also observed using the MIPS camera in SED mode, which provides very low resolution ($R \sim 20$) slit spectroscopy covering $\sim \lambda_{55-90} \mu\text{m}$. The slit-width for SED mode observations is $20''$. Integration times ranged from 3 to 10 seconds depending on the IRAS $60\mu\text{m}$ flux density. Observations include six pairs of on-source and

off-source positions (1-3' away from source) for background subtraction.

Basic data processing, including background subtraction and flux and wavelength calibration, was handled by the *Spitzer* pipeline (version S.14.4). The final, low resolution spectra were extracted from the long-slit images using a three-pixel ($\sim 30''$) synthetic aperture perpendicular to the slit. For each source, the position of the galaxy nucleus was identified first manually and then by a Gaussian fit to determine the center of the extraction aperture to a fraction of a pixel.

Note that flux calibration is derived from observations of standard stars and so is most accurate for compact far-infrared sources. Formally, the accuracy for point sources is better than 10%, but degrades to $\sim 15\%$ for extended sources with galaxy-like surface brightness profiles (Lu et al. 2008).

2.4. PAHFIT Spectral Decomposition

We used the PAHFIT spectral decomposition code (Smith et al. 2007a) to fit and extract line features of the Seyfert IRS spectra. The publicly available release of PAHFIT permits silicate features only in absorption. Silicate $10\ \mu\text{m}$ and $18\ \mu\text{m}$ emission commonly appears among the sample, however, and we therefore modified PAHFIT to include a warm, optically thin ($\tau(10\ \mu\text{m}) < 1$) dusty medium. To accommodate the range of observed Sil emission profiles, the warm dust model includes two components: (1) an optically thin warm medium, characterized by a single temperature and $10\ \mu\text{m}$ opacity, and (2) a cold, partially covering dusty medium parameterized solely by covering fraction (i.e., the cold dust is modeled to produce no significant emission over the IRS band). Both the cold and warm dust components obey the extinction law described by Smith et al. (2007a). Our goal was to reproduce the observed silicate emission profile shapes without regard to determining the physics of the warm dust (other than its presence and emission strength), and so, for simplicity, the spectrum of the warm dust, modified by partial foreground absorber, was calculated assuming a simple slab geometry.

Except for this added warm dust component, we used PAHFIT with its default settings. PAHFIT robustly decomposes the spectrum into multiple temperature dust components, silicate features, emission lines, and PAH dust features. The decomposition proceeds using a standard non-linear fitting algorithm. PAHFIT was specifically designed to analyze moderate resolution IRS spectra and carefully limits parameters, such as line widths and centroids, that might drift to unphysical values during the fit.

The final data products include tables of line strengths and equivalent widths. We

further modified PAHFIT to produce line-subtracted continua. These continua were used to calculate silicate strengths and spectral indices. In addition, we also modified the PAHFIT output to produce 3σ upper limits for weak or undetected lines. These data tables are provided in Gallimore et al. (2009a). Note that the line and feature fluxes are not corrected for extinction.

Table 1 summarizes the results of the PAHFIT decomposition, giving the median values of a range of properties for the continuum emission, Sil feature, star formation tracers, AGN tracers, and diagnostic line ratios. The median values were calculated based on the computation of a survival curve (Feigelson & Nelson 1985). As the line ratios include both upper and lower limits, we employed the formalism for interval-censoring given by Finkelstein (1986) and Sun (1996), as implemented in the interval package by M. P. Fay & P. A. Shaw (<http://cran.r-project.org/web/packages/interval/index.html>).

Tables 2-9 give the results of statistical tests for the significance of differences in the distribution of those properties for the different Seyfert subgroups. These tests comprise Kolmogorov-Smirnov two-sample tests for uncensored data, or log-rank tests for interval-censored data.

Table 10 gives the significance of rank correlations between the properties for the combined sample. We used Kendall’s rank correlation statistic adapted for interval-censored data (Isobe, Feigelson, & Nelson 1986), reported as a z -score and two-sided significance level.

In this paper, we search extensively for patterns in the data by exploring bivariate correlations among measurements: for example, PAH eqw vs. 20–30 μm spectral index. There are well-known parametric and non-parametric statistical measures of correlation (see, e.g., Sprent & Smeeton 2000). Parametric methods specifically apply to cases where the data are believed to be related through some known and prescribed functional form; for example, the well-known Pearson correlation coefficient measures the underlying linear relationship between measurements. One however expects a fairly complex relationship, if at all, between a spectral index and an eqw, and so such parametric statistics would not be expected to apply in the present analyses. For example, data that are tightly but non-linearly correlated will likely show low linear correlation measurements (Anscombe 1973).

In contrast, rank correlation coefficients provide a robust, non-parametric measure of association between measurements. They are better suited for the present study, as they measure simply the degree to which one measurement increases (or decreases) as another increases, independent of the degree or functional form of the underlying association. To our knowledge, only Kendall’s rank correlation statistic (Kendall’s τ ; (Kendall 1938)) has been generalized to account both for upper limits (non-detections) and lower limits (e.g., line

ratios where the divisor is an upper limit) in one or both measurements and so is ideal for this study. We have implemented the generalized Kendall’s rank correlation statistic following the formalism of Isobe, Feigelson, & Nelson (1986). In the results tables, we report the standard normal score (z) of the statistic as well as the probability (p) that score would have occurred by chance (i.e., the probability of no correlation). We chose to be conservative in the interpretation of the correlation statistics and adopt the threshold $p < 1\%$ to indicate evidence of rank correlation.

3. RESULTS

3.1. The Starburst AGN Connection

3.1.1. PAH Emission as a diagnostic of Star Formation

The PAH emission is thought to be produced when small grains (containing ~ 50 Carbon atoms) are heated by single UV photons from hot stars and radiate through their vibrational modes (Tielens et al. 1999). It is clear that PAH emission is a tracer of star forming regions in our Galaxy (Tielens et al. 1999) and other galaxies (Laurent et al. 2000; Peeters et al. 2004; Brandl et al. 2006; Dale et al. 2006; Draine et al. 2007; Smith et al. 2007a). The PAH luminosity is proportional to the star formation rate in star forming galaxies (Roussel et al. 2001; Brandl et al. 2006; Calzetti et al. 2007; Shi et al. 2007; Farrah et al. 2007). Voit (1992a) argues that PAH grains exposed to the direct hard continuum of an AGN will be destroyed, and the PAHs in AGN can only survive when they are shielded by high columns of X-ray absorbing gas, e.g., in the plane of the obscuring torus. Smith et al. (2007a) notes that the ratio of 7.7/11.3 micron PAH seems to be lower in some AGN than in starburst galaxies. Since the 11.3 micron PAH are produced by larger grains than the 7.7 micron PAH (Draine & Li 2007) this suggests that the smaller grains are indeed being destroyed by the AGN. Thus, PAH emission seems to be a good indicator of star formation in galaxies with the caveat that it may be significantly suppressed in AGN. Siebenmorgen, Krügel & Spoon (2004) compare radiative transfer models which include dust destruction for starbursts and AGN. In their models, some PAH emission is produced within clouds illuminated by an AGN, but the strength of the PAH is lower by a factor of about 5 than that produced in the starburst models with the same luminosity and A_v . Finally, the equivalent width of PAH features has been shown to be useful in diagnostic diagrams as a discriminant between starbursts and AGN as the energy source for infrared emission (Genzel et al. 1998; Laurent et al. 2000; Peeters et al. 2004; Armus et al. 2007; Spoon et al. 2007).

The 6.2 micron PAH feature is thought to be relatively “unconfused” by other spectral

features (e.g., Peeters *et al.* 2004) and so should be a good measure of the amount of star formation. We show the distribution of $6.2 \mu\text{m}$ PAH EW for the Sy 1's, Sy 2's and hidden Sy 1's in Figure 1. We see that the Sy 2s show a distribution to higher values of PAH EW. We find that the distribution of PAH EW in the Sy 1's and Sy 2's are significantly different (Table 2) in contrast to Wu *et al.* (2009) who find no significant difference in the EWs. This might be due to the systematic differences in the measured PAH EWs discussed by Gallimore *et al.* (2009a). The Sy 2's which show the high EW are those without an HBLR; the Sy 2's with an HBLR have a distribution which is similar to that of the Sy 1's (Tables 1, 2,3). The higher values of PAH EW for the Sy 2s seems mainly due to the lower continuum fluxes in the Sy 2's relative to the Sy 1's since the PAH *luminosities* (Figure 2) are similar in the Sy 2's and the Sy 1's. This result is consistent with the findings of Clavel *et al.* (2000) for a sample of Seyferts studied using ISO. Figures 1 and 2 also show that the Seyferts show a similar distribution in $6.2 \mu\text{m}$ PAH luminosity as the Brandl *et al.* (2006) starbursts. However, the Seyferts show lower $6.2 \mu\text{m}$ PAH EW due to the higher continuum contribution from the AGN. These results are consistent with the results of Buchanan *et al.* (2006) that principle component analysis required a higher star formation contribution to the SED of Sy 2's.

3.1.2. The PAH 6.2/11.3 ratio

The $6.2 \mu\text{m}$ PAH feature is produced by grains with smaller sizes than the $11.3 \mu\text{m}$ PAH feature (Draine & Li 2007). The smaller grains are more quickly destroyed by exposure to the AGN spectrum. Thus, the ratio of 6.2/11.3 PAH should be an indicator of the destruction of grains by the AGN (Smith *et al.* 2007a). Wu *et al.* (2009) show that their Seyfert sample and the Brandl *et al.* (2006) sample of starburst galaxies have similar average values for the 11.3/6.2 PAH ratio.

We calculate the 6.2/11.3 PAH ratio using the fluxes of the features. The distribution of the 6.2/11.3 PAH ratio is consistent with being the same in the different subgroups. In Figure 3 we plot the ratio of the 6.2 and $11.3 \mu\text{m}$ PAH strength vs. the [NeV] luminosity which traces the strength of the AGN ionizing continuum (§ 3.1.6). We see no correlation of the PAH ratio with the [NeV] luminosity. In Figure 4 we plot the 6.2/11.3 PAH ratio against the Sil $10 \mu\text{m}$ Strength (see §3.2.1). We do not see a correlation between the PAH ratio and the Sil $10 \mu\text{m}$ Strength (Table 10). This suggests that the PAH emission that we see in these Seyferts is not orientation dependent. Any effect of the AGN on the distribution of PAH grains must be confined to a small volume so that the integrated measurements studied here are not affected.

3.1.3. PAH Associated with Emission from Cool Dust

Schweitzer et al. (2006) show that QSOs and ULIRGs lie on the same correlation between $7.7 \mu\text{m}$ PAH flux and $60 \mu\text{m}$ continuum flux, suggesting that the FIR is dominated by dust heated by star formation. In Figure 5 we show a strong rank correlation between $6.2 \mu\text{m}$ PAH luminosity and the integrated luminosity (from IRAS) at $60 \mu\text{m}$ for our sample. We also find a rank correlation between the *flux* of the $6.2 \mu\text{m}$ PAH feature and the $60 \mu\text{m}$ continuum (Table 10).

We also show the $6.2 \mu\text{m}$ PAH EW vs. the spectral index of the MIPS SED $55\text{-}90 \mu\text{m}$ in Figure 6. The slope of the MIPS SED indicates the relative importance of cold vs. warm dust to the FIR SED. Positive slope is a red MFIR SED. The starburst galaxies all lie at large PAH EW. In the combined sample, we see a rank correlation between PAH EW and MIPS slope, with higher PAH strength (more star formation) proportional to more positive (redder) MIPS slope (more emission from cool dust). These two correlations (Figures 5 and 6) are consistent with a significant contribution from stars to the heating of the cool dust which produces the FIR emission in our sample.

3.1.4. PAH EW vs. 20-30 μm spectral index: a measure of the relative strength of the starburst and AGN components

20 microns is just redward of the “knee bend” we see in the SED of many Sy 1s and 2s (Buchanan et al. 2006). The 20-30 micron spectral index α_{20-30} , was determined using a power law fit to the line-subtracted continuum between 20 and 30 microns rest frame. This spectral index characterizes the relative contribution of warm and cool dust to the mid-IR. Note that the values of α_{20-30} used in Buchanan et al. (2006) are actually $\alpha_{20-30} + 2.0$. The correct values of α_{20-30} are used here. The similar 15-30 μm spectral index has also been found to be an effective AGN discriminator (Brandl et al. 2006; Cleary et al. 2007). Using a subset of our data, Deo et al. (2007) show that there is a correlation between the $6.2 \mu\text{m}$ PAH EW and α_{20-30} . Wu et al. (2009) also find a correlation between the the $11.3 \mu\text{m}$ PAH EW and the 15-30 μm spectral index. We plot the $6.2 \mu\text{m}$ PAH EW vs. α_{20-30} in Figure 7. We see the different subsamples tend to lie in different parts of the diagram. The Sy 1’s and Sy 2’s with an HBLR generally have $\alpha_{20-30} < -0.5$ and cover a large range in $6.2 \mu\text{m}$ PAH EW. On the other hand the Sy 2’s and Liners tend to have high values of $6.2 \mu\text{m}$ PAH EW and cover a large range in α_{20-30} with the Sy 2’s showing a strong rank correlation ($p < 0.1\%$) between the two properties. We also see a rank correlation between $6.2 \mu\text{m}$ PAH *Luminosity* and α_{20-30} (Figure 8). Thus we see rank correlations between the PAH EW and α_{20-30} which are both measures of the *relative* strength of the starburst and AGN

components, and also PAH luminosity (a measure of the absolute strength of the starburst component) and α_{20-30} .

In Figure 7 the sources in the lower left are those with a low starburst to AGN ratio. Thus, the value of α_{20-30} between -1 and -2 is likely to represent the spectrum of the “torus”, consistent with values calculated by Nenkova et al. (2008).

In Figure 9 we plot the 55-90 μm spectral index vs. 20-30 μm spectral index. We see a correlation in the sense that objects which are redder in 20-30 tend to be redder in 55-90. This is consistent with the hypothesis that star formation contributes to both the 20-30 and 55-90 spectral regions. Thus, the 55-90 vs. 20-30 spectral index plot is also a diagnostic of the relative contribution of Starburst to AGN. We see there is a large range in spectral index across the sample: $\Delta\alpha \sim 3$ for both indexes. Thus, the contribution to the IR spectrum from the AGN and starburst components can be comparable in magnitude but the relative contribution also varies widely across the sample (see also Buchanan et al. 2006; Deo et al. 2007; Wu et al. 2009).

3.1.5. *The Relationship between Molecular Hydrogen and Star Formation*

Figure 10 shows the 6.2 μm PAH EW vs. the $\text{H}_2 S(1)$ 17 μm EW. The $\text{H}_2 S(1)$ line has higher EW in the Starbursts and Liners than the Seyferts. The distribution of the fluxes and luminosities of the $\text{H}_2 S(1)$ 17 μm line are consistent with being the same in the subclasses of Seyferts (Tables 2-8).

We see that the $\text{H}_2 S(1)$ EW is proportional to the PAH EW. Tommasin et al. (2008) show a correlation between the luminosities of the 11.3 μm PAH and $\text{H}_2 S(1)$ 17 μm lines in a subsample of these sources. We also find a rank correlation between the luminosities of the 6.2 μm PAH and the $\text{H}_2 S(1)$ 17 μm line (a rank correlation is also found in the fluxes; Table 10). We note that Schweitzer et al. (2006) have also reported a correlation between PAH and H_2 in the higher luminosity QUEST QSOs. Since the PAH is a tracer of star formation this suggests that the H_2 line is also associated with star formation.

In Figure 11 we plot α_{20-30} vs. the $\text{H}_2 S(1)$ 17 μm EW. We see a correlation in the sense that objects with redder continuum slopes have larger $\text{H}_2 S(1)$ EW. Since red continua are associated with cold dust from stars, this correlation is also consistent with the molecular hydrogen line being associated with star formation.

3.1.6. AGN Tracers

Following Voit (1992b) and Spinoglio & Malkan (1992), we adopt the high ionization lines [NeV] (97.1 eV) and [OIV] (54.9 eV) as tracers of the AGN in these objects. The vast majority of stars do not produce photons sufficiently energetic to excite [NeV] and [OIV], with the exception of young Wolf-Rayet stars (Schaerer & Stasińska 1999). However, Abel & Satyapal (2008) show that even in AGN with a strong starburst component, the observed ionization parameters constrain the [NeV] emission to be dominated by the AGN.

It is also possible for [NeV] and [OIV] to be excited by shocks with velocities > 200 km s⁻¹ (Allen et al. 2008). However, as Allen et al. note, the predicted line ratios are not in agreement with observations. Detailed studies of the IR spectrum of Seyferts are instead consistent with AGN photoionization of the NLR (Groves, Dopita & Sutherland 2006). In addition, the line ratios [NeV]/[NeII] and [OIV]/[NeII] have proved empirically to provide good separation between AGN and Starbursts (Genzel et al. 1998; Sturm et al. 2002, 2006). And the [OIV]26 μ m line has also shown to be correlated with other AGN tracers - the [OIII] λ 5007 line, radio emission, and the 2-10 keV X-ray flux in other samples (Meléndez et al. 2008; Diamond-Stanic et al. 2009).

In Figure 12 we show a rank correlation between the luminosity of the [NeV] 14 μ m line and the 8.4 GHz radio continuum. A rank correlation is also present between the *fluxes* of the [NeV] 14 μ m line and the 8.4 GHz radio continuum (Table 10). The 8.4 GHz radio emission is not orientation dependent (Thean et al. 2001) and is an unbiased measure of the isotropic AGN luminosity. The rank correlation of the [NeV] 14 μ m line with the 8 GHz radio emission suggests that the [NeV] line emission is also a useful measure of AGN luminosity (see also § 3.2.3).

In models of the obscuring torus, the flux in the near-mid IR (i.e., $\sim 3 - 10\mu$ m) is due to hot dust heated by the AGN (Pier & Krolik 1992; Granato & Danese 1994; Efstathiou & Rowan-Robinson 1995; van Bemmelen & Dullemond 2003; Nenkova et al. 2002, 2008). Thus, we adopt the 6.7 μ m continuum flux as an AGN tracer. In § 3.2.4 we show a rank correlation between the 6.7 μ m continuum and the [NeV] 14 μ m line emission.

In Figure 13 we see rank correlations between the luminosities of the two IR AGN tracers the [NeV] 14 μ m and [OIV] 26 μ m lines with the optical [OIII] λ 5007 line ([OIII] measurements taken from (Axon 2009 private communication; Deo et al. 2007; de Grijp et al. 1992; Gu et al. 2006; Kewley et al. 2001; Kim et al. 1995; Kirhakos & Steiner 1990; Meléndez et al. 2008; Panessa & Bassani 2002; Smith et al. 2002; Tran 2003; Véron-Cetty & Véron 2001; Winkler 1992; Whittle 1992; Young et al. 1996)). The rank correlations are also present but weaker between the fluxes of the lines. This confirms that the [NeV] 14 μ m and [OIV]

26 μm are useful AGN tracers.

3.1.7. Comparison of Starburst and AGN Tracers

Correlations between AGN and starburst tracers have been found for QSOs (Haas et al. 2003; Schweitzer et al. 2006; Netzer et al. 2007; Maiolino et al. 2007) and Seyferts (Maiolino et al. 2007). Figure 14 shows a rank correlation between the luminosities of the 6.2 μm PAH and the [NeV] 14 μm line in the combined sample. We also find rank correlations between the luminosities of (1) the 6.2 μm PAH and the [OIV] 26 μm line (2) the [NeV] 14 μm line and the 60 μm continuum, and (3) the 6.2 μm PAH feature and the 6.7 μm continuum (not plotted, see Table 10). These correlations seem to indicate that the starburst and AGN luminosities are correlated in these Seyferts. However, our statistical tests (Table 10) show that there are no significant correlations in the *flux* of these AGN and Starburst tracers. Figure 15 shows that the fluxes of the 6.2 μm PAH and [NeV] 14 μm line scatter over an order of magnitude and are uncorrelated. So although AGN tracers are internally correlated in both flux and luminosity, and Starburst tracers are internally correlated in both flux and luminosity, the fluxes of the AGN and Starburst tracers are not correlated. We conclude that the correlations in Starburst and AGN luminosity are due to the dependence on distance and are not real. This is consistent with our results that the relative strength of the AGN and Starburst components in these Seyferts vary widely across the sample (§ 3.1.4). The lack of a correlation between the AGN and star burst suggests that in these AGN there is no direct link between AGN fueling, black hole growth, and star formation.

3.1.8. The [NeV]/[NeII] ratio vs. PAH EW Diagram

Genzel et al. (1998) showed that a diagram which plots the ratio of a high to low ionization line vs. a PAH EW is able to separate Starbursts from AGN from ULIRGs. Genzel et al. (1998) used [OIV]/NeII vs. the 7.7 μm PAH EW. In Figure 16 we plot 6.2 μm PAH EW vs. [NeV]14 μm /[NeII]12 μm . We see that there are significant differences across our sample with objects with higher AGN to starburst ratio in the lower right and the objects with lower AGN to starburst ratio in the upper left. Note that the Liners have low [NeV]14 μm /[NeII]12 μm and tend to fall to the left of the other objects.

3.2. Orientation, Obscuration, and Constraints on the Torus

3.2.1. 6.2 μm PAH vs. Sil 10 μm Strength

The strength of the Sil 10 μm feature is potentially a powerful probe of the absorbing material (Pier & Krolik 1992; Laor & Draine 1993; Levenson et al. 2007; Imanishi et al. 2007). We adopt the definition of Sil strength given by Spoon et al. (2007),

$$S_{\text{Sil}} = \ln \frac{f_{\text{obs}}(10)}{f_{\text{cont}}(10)} \quad (1)$$

where f_{obs} is the observed flux in the feature and f_{cont} is the interpolated continuum flux at 10 μm . Recent Spitzer results suggest that different types of objects show systematically different Sil 10 μm strength (Shi et al. 2006; Hao et al. 2007) with QSOs showing strong Sil emission, Sy 1s showing mostly weak Sil emission, Sy 2s showing mostly weak to moderate Sil absorption, and ULIRGS showing strong Sil absorption. Spoon et al. (2007) have shown that objects fall mainly in two branches on the 6.2 μm PAH vs. Sil 10 μm Strength diagram.

Figure 17 shows the distribution on the 6.2 μm PAH vs. Sil 10 μm Strength diagram. Our results are consistent with those of Spoon et al. (2007). As expected, the Sy 1's tend to show weak Sil emission, and the Sy 2's tend to show Sil absorption. The KS test (Table 2) confirms that the distribution of Sil strength is very different in the Sy 1's and Sy 2's. These results are in qualitative agreement with Wu et al. (2009), though as discussed by Gallimore et al. (2009a) there are systematic differences in the measured Sil strengths. The only significant difference between the Sy 1's and the Sy 2's with an HBLR is the Sil strength (Table 5).

Two of the HBLR Sy 2's show Sil emission - F01475-0740 and M-3-58-7. In these objects, the obscuring material (torus) may be oriented at an intermediate inclination. In addition, four objects classified as S1.8-1.9 show Sil absorption - NGC1194 (S1.9), M-2-40-4 (Sy1.9), NGC1365 (S1.8), and NGC5033 (S1.8). These are also likely to be fairly edge-on (§ 3.3). About half of the objects identified as Liners and Starbursts show weak Sil features, with strong absorption seen in MRK938 (HII), NGC3079 (LINER), NGC5005 (LINER), and strong emission seen in NGC4579 (LINER), NGC5494 (LINER), and CGCG381-051 (HII).

3.2.2. Sil 10 μm Strength vs. Sil 18 μm Strength

Sirocky et al. (2008) showed that the observed relationship between the two Sil features 18 μm and 10 μm can be a powerful probe of the properties of the obscuring material. Figure 18 shows the distribution of the Sil strengths for the different subsamples of galaxies.

We see the Sy 1's mainly to the upper right with emission in both Sil features, and the Sy 2's mainly to the lower left with absorption in both Sil features. In Figure 19 we compare our results for the two Sil Strength features with simple spherical obscuration models (Sirocky et al. 2008). The spherical models have the advantage that they reduce the number of free parameters and still give good agreement with the more detailed clumpy torus models (Nenkova et al. 2002, 2008). We see that the data lie below the smooth torus models and within the parameter space of the clumpy torus models. Our data are inconsistent with the smooth torus models but are consistent with the clumpy torus models. Within the context of the spherical clumpy models, there is a preference for a small number of clumps along the line of sight ($N \sim 1 - 3$).

3.2.3. Density and Obscuration Diagnostics

The [NeV] 14/24 and [SIII] 18/33 line ratios are density diagnostics (Voit 1992b; Spinoglio & Malkan 1992), and in principle, in the low density limit can be used as extinction indicators (Voit 1992b; Alexander et al. 1999; Dudik et al. 2007). The [NeV] lines will probe high excitation gas, most likely in the narrow line region, while the [SIII] can be excited by stars and may be produced on a larger spatial scale. Sturm et al (2002) examined the [NeV] 14/24 ratio in a sample of Seyferts using ISO data and also concluded that the [NeV] emitting gas in both Seyfert types was in the low density limit. On the other hand Dudik et al. (2007) find that type 2 AGNs tend to have lower ratios than type 1 AGN, and some of the type 2 AGNs are below the low density limit possibly due to differential absorption. Tommasin *et al.* (2008) using high resolution IRS spectra on a subsample of the 12 μm sample, report [NeV] line ratios slightly above the low density limit, giving densities of $n_e \sim 10^3 \text{ cm}^{-3}$.

Our data (Figure 20) and Tables 1 - 5) are consistent with Sy 1's, Sy 2's and hidden Sy 1's having the same distribution of these diagnostic ratios. Both line ratios seem to scatter around their low density values giving for [NeV] $n_e \sim 10^3 \text{ cm}^{-3}$ and for [SIII], $n_e \sim \text{few hundred cm}^{-3}$. We also see no evidence for a correlation between the values of these ratios (Table 10).

In Figure 21 we plot the [NeV] 14/24 line ratio against the Sil 10 μm feature which is an indicator of absorption along the line of sight (§3.2.1). We see that there is no correlation between these two quantities (Table 10). This suggests that extinction does not have a significant effect on the observed [NeV] 14/24 line ratio.

In Figure 22 we show the [NeV] 14 μm EW vs. Sil 10 μm Strength. We see that the

distribution of [NeV] EW is similar in Sy 1’s, Sy 2’s and hidden Sy 1’s (Table 2, 3,4,5). There is no correlation of [NeV] EW or luminosity with Sil strength (Table 10). This is consistent with our results above that (1) the [NeV] luminosity is proportional to the radio power, and (2) the effect of extinction on the [NeV] 14/24 ratio is small. This suggests that either the torus is not very opaque at these wavelengths (14-24 μm), or [NeV] is produced primarily outside the torus, e.g., in the NLR. However, we expect the high ionization lines [NeV] and [OIII] to be produced in similar locations around the AGN.

Haas et al. (2005) have shown that [OIII] is very orientation dependent in quasars and radio galaxies, suggesting that much of the [OIII] is produced in regions obscured by the torus. In Figure 23 we show the ratios [OIII] λ 5007/[OIV]26 μm and [OIII] λ 5007/[NeV]14 μm vs. the Sil Strength. We see a strong rank correlation for [OIII] λ 5007/[OIV]26 μm and a weaker one for [OIII] λ 5007/[NeV]14 μm in the sense that the ratio is higher in objects with Sil emission (roughly face on) and lower in objects with Sil absorption (roughly edge on). We find that [OIII] is orientation dependent in our sample of Seyferts suggesting that much of the [OIII] emission is produced in a region which is subject to orientation dependent obscuration, e.g., the torus. Thus, if [NeV] is also primarily produced in regions obscured by the torus, then our result suggests that the opacity of the torus at 14 μm is not large. This is consistent with the results of Buchanan et al. (2006).

3.2.4. *An Extended Hot Dust Component in Seyferts?*

High resolution mid-IR observations show extended hot dust associated with the NLR in NGC1068 (Galliano et al. 2005; Mason et al. 2006) and the Circinus galaxy (Packham et al. 2005). Figure 24 shows a rank correlation between the luminosities in the [NeV] 14 μm line and the continuum determined at 6.7 μm in our Seyferts. The rank correlation is also present between the fluxes (Table 10). In § 3.2.3 we show that the [NeV] emission is not strongly orientation dependent. However, in models where the 6.7 μm continuum originates in the hot dust in the inner torus, we would expect the 6.7 μm continuum to be orientation dependent. In the context of standard uniform torus models we would expect that the 6.7 μm emission should be high in the Sy 1’s, but low in the Sy 2’s where it is obscured by the torus. Instead we see a strong rank correlation followed by both Sy 1’s and Sy 2’s. This suggests that in addition to any hot dust in the torus, we are seeing an extended component of hot dust whose luminosity scales with the AGN luminosity (as measured by [NeV]). This might be due to dust in the NLR or a wind. Mor et al. (2009) also find evidence for hot dust emission associated with the NLR in luminous QSOs.

3.3. Comparison of Seyfert Subsamples

Here we discuss the properties of subsamples of the Seyfert population. Table 1 gives the median values of a range of properties for the continuum emission, Sil feature, star formation tracers, AGN tracers, and diagnostic line ratios. Tables 2-9 give the results of statistical tests for the significance of differences in the distribution of those properties.

The comparison of the Sy 1’s with the Sy 2’s (both with and without a detected HBLR) (Table 2) shows significant differences ($p < 1\%$) between the Sil feature, the 20-30 μm spectral index, 6.7 μm continuum flux density, and the EW of the 6.2 μm PAH feature. As discussed in §3.2.1, the Sy 1’s exhibit weak Sil emission and the Sy 2’s show Sil absorption. The other differences are consistent with being due to a higher contribution from hot dust in the spectra of the Sy 1’s which causes higher 6.7 μm continuum, bluer 20-30 μm spectral index, and lower EW of the 6.2 μm PAH feature. Note that although the EWs are different, the luminosities are similar. When we compare the Sy 1’s to just those Sy 2’s without an HBLR (Table 3) we see the same differences as between the Sy 1’s and all the Sy 2’s, with the addition of a difference in the luminosity of the 6.7 μm continuum.

The Sy 2’s with and without HBLRs show differences in 20-30 μm spectral index, 6.7 μm continuum, and EW of the 6.2 μm PAH feature and the $\text{H}_2 S(1)$ line (Table 4). These differences are consistent with a higher contribution from a hot dust component in the HBLR Sy 2’s. In addition, the Sy 2’s with an HBLR are very similar to the the Sy 1’s; the only significant difference is the Sil strength (Table 5). Thus, the Sy 2’s with an HBLR are more similar to the Sy 1’s than they are to the Sy 2’s without an HBLR. The differences are in the sense that the Sy 2’s with an HBLR have a higher ratio of AGN to Starburst contribution to the SED. This may contribute to the detection of the HBLR in polarized light. This is consistent with Alexander (2001) who noted that there was a weaker contribution from the galaxy in the HBLR Sy 2’s than the non-HBLR Sy 2’s. We cannot rule out the possibility that the differences between the HBLR and non-HBLR Sy 2’s reflect intrinsic differences in the AGN.

Deo et al. (2007) find that the mid-IR spectra of Sy 1.8-1.9 and are similar to those of Sy 2’s with significant star formation. The Sy 1.8–1.9 are the smallest subgroup with only six objects in this study. The statistics are of course severely affected by small numbers, but we include the analyses for completeness. The Sy 1.8–1.9 show no significant differences with the Sy 2’s without an HBLR (Table 6) or with an HBLR (Table 7). or the Sy 1’s (Table 8). This lack of difference between the Sy 1.8–1.9 and the other Seyfert types suggests that the Sy 1.8-1.9 may have intermediate properties between the Sy 1’s and Sy 2’s (as suggested by Deo et al. (2007)). However, it may also be due to the small number of Sy 1.8–1.9 in this study.

As noted above Sy 1.8-1.9 have mid-IR spectra which are similar to those of Sy 2's (Deo et al. 2007) and HBLR Sy 2's have mid-IR spectra which are closer to those of Sy 1's than non-HBLR Sy 2's. Thus, we also created a modified class of AGN1 consisting of the Sy 1's plus the Sy 2's with an HBLR, and a modified class of AGN2 consisting of the Sy 2's without an HBLR plus the Sy 1.8-1.9. The test for differences in the properties of these two modified classes is shown in Table 9. We compare these results (Table 9) to the comparison between the Sy 1's and Sy 2's (Table 2). In the modified AGN1 and AGN2 the differences in 20-30 μm spectral index, 6.7 μm continuum flux and luminosity, and EW of the 6.2 μm PAH feature are stronger; the differences in Sil strength are weaker; and the modified samples show a new difference in the EW of the $\text{H}_2 S(1)$ line. These findings are consistent with our results that the Sy 2's with an HBLR have a larger contribution from a hot dust component than the the Sy 2's without an HBLR.

4. SUMMARY

We present an analysis of Spitzer IRS spectroscopy of 83 active galaxies, including 73 Seyferts, 6 LINERS, and 4 HII galaxies from the extended 12 μm sample of Rush et al. (1993). We fit the spectra using a modified version of the Smith et al. (2007a) PAHFIT program and examine selected diagnostic spectral features.

Sy 1's and Sy 2's and the Brandl et al. (2006) sample of starbursts have similar distributions of the luminosity of the 6.2 μm PAH feature. The EW of the 6.2 μm PAH feature is slightly larger in the Sy 2's and much larger in the Brandl et al. (2006) sample of starbursts than in the Sy 1's due to the differences in the underlying continuum.

We see no difference in the 6.2/11.3 PAH ratio between the different sub samples or any dependence of the ratio on [NeV] luminosity or Sil 10 μm strength. Thus, any effect of the AGN on the distribution of PAH grains must be confined to a small volume so that the integrated measurements studied here are not affected.

The PAH EW is larger in sources with redder mid and far IR spectra. In addition, the luminosity of the 6.2 μm PAH feature is rank correlated with the luminosity of the continuum at 60 μm . The correlation is also present in the fluxes. Both of these results suggest that (1) The PAH feature is a reliable tracer of star formation and (2) there is a significant contribution to the heating of the cool dust by stars. The 55-90 vs. 20-30 spectral index plot is also a diagnostic of the relative contribution of Starburst to AGN. We see there is a large change in spectral index across the sample: $\Delta\alpha \sim 3$ for both indexes. Thus, the contribution to the IR spectrum from the AGN and starburst components can be comparable

in magnitude but the relative contribution also varies widely across the sample.

We see a rank correlation between the $H_2S(1)$ $17\ \mu\text{m}$ EW and two measures of the relative strength of the Starburst to AGN component - the $6.2\ \mu\text{m}$ PAH EW and the $20\text{--}30\ \mu\text{m}$ spectral index. We also see a rank correlation between the luminosities of the $6.2\ \mu\text{m}$ PAH feature and the $H_2S(1)$ $17\ \mu\text{m}$ line. The rank correlation is also present in the fluxes. These results suggest that the H_2 emission is also primarily excited by star formation.

We find rank correlations between several AGN tracers - $8\ \text{GHz}$ vs. $[\text{NeV}]14\ \mu\text{m}$ $[\text{NeV}]14\ \mu\text{m}$ vs. $[\text{OIII}]\lambda 5007$, $[\text{OIV}]26\ \mu\text{m}$ vs. $[\text{OIII}]\lambda 5007$, and $[\text{NeV}]14\ \mu\text{m}$ vs. $6.7\ \mu\text{m}$ continuum. The correlations are present both in the fluxes and luminosities of these AGN tracers. The rank correlation between $[\text{NeV}]14\ \mu\text{m}$ vs. $6.7\ \mu\text{m}$ continuum suggests that there is a component to the $6.7\ \mu\text{m}$ continuum from hot dust which is extended, e.g., in the NLR. We find rank correlations of the ratios $[\text{OIII}]\lambda 5007/[\text{OIV}]26\ \mu\text{m}$ and $[\text{OIII}]\lambda 5007/[\text{NeV}]14\ \mu\text{m}$ with the Sil strength orientation indicator. This suggests that some of the $[\text{OIII}]\lambda 5007$ emission in these Seyferts is subject to orientation dependent obscuration as found by Haas et al. (2005) for radio galaxies and quasars. There is no correlation of $[\text{NeV}]$ EW with the orientation indicator Sil $10\ \mu\text{m}$ strength indicating that the $[\text{NeV}]$ emission is not strongly orientation dependent. This suggests with the obscuring material (e.g., torus) is not very optically thick at $14\ \mu\text{m}$ consistent with the results of Buchanan et al. (2006).

We searched for correlations between AGN and Starburst tracers (i.e., $6.2\ \mu\text{m}$ PAH vs. $[\text{NeV}] 14\ \mu\text{m}$ or $[\text{OIV}] 26\ \mu\text{m}$ or $6.7\ \mu\text{m}$ continuum, and $[\text{NeV}] 14\ \mu\text{m}$ vs. $60\ \mu\text{m}$ continuum). Although there are apparent correlations in luminosity (likely due to the dependence on distance), there are no significant correlations in flux, and we conclude that the AGN and Starburst tracers are not correlated. This is consistent with our conclusion that the relative strength of the AGN and Starburst components varies widely across the sample. The lack of a correlation between the AGN and star burst suggests that in these AGN there is no direct link between AGN fueling, black hole growth, and star formation.

The density diagnostic $[\text{NeV}] 14/24\ \mu\text{m}$ and $[\text{SIII}] 18/33\ \mu\text{m}$ line ratios are consistent with the gas being near the low density limit, i.e., $\sim 10^3\ \text{cm}^{-3}$ for $[\text{NeV}]$ and $n_e \sim \text{few hundred}\ \text{cm}^{-3}$ for $[\text{SIII}]$.

The distribution of Sil $10\ \mu\text{m}$ and $18\ \mu\text{m}$ strengths is consistent with the clumpy torus models of Sirocky et al. (2008).

We find a rank correlation between the $[\text{NeV}] 14\ \mu\text{m}$ line and the continuum determined at $6.7\ \mu\text{m}$ in our Seyferts. This suggests that in addition to any hot dust in the torus, we are seeing an extended component of hot dust whose luminosity scales with the AGN luminosity (as measured by $[\text{NeV}]$). This might be due to dust in the NLR or a wind.

We have compared the distribution of several starburst and AGN tracers between the different subsamples of Seyferts. Our comparison of the Sy 1's with the Sy 2's without an HBLR shows that in addition to the strong difference in the Sil strength, the Sy 2's without an HBLR have $2 - 3\sigma$ differences in the 20-30 μm spectral index, 6.7 μm continuum, and the EW of the 6.2 μm PAH feature and [NeV] 14 μm line. The Sy 2's with an HBLR have similar distributions of properties to the Sy 1's; the only significant difference is the Sil strength. Thus, the Sy 2's with an HBLR are more similar to the Sy 1's than they are to the Sy 2's without an HBLR. The differences are in the sense that the Sy 2's with an HBLR have a higher ratio of AGN to Starburst contribution to the SED. This may contribute to the detection of the HBLR in polarized light. This is consistent with Alexander (2001) who noted that there was a weaker contribution from the galaxy in the HBLR Sy 2's than the non-HBLR Sy 2's.

This work is based in part on observations made with the Spitzer Space Telescope, which is operated by the Jet Propulsion Laboratory, California Institute of Technology under a contract with NASA. Support for this work at Bucknell University and Rochester Institute of Technology was provided by NASA through an award issued by JPL/Caltech. We are grateful to Henrik Spoon for helpful discussions and to an anonymous referee for constructive comments. This research made use of (1) the NASA/IPAC Extragalactic Database (NED), which is operated by the Jet Propulsion Laboratory, California Institute of Technology, under contract with the National Aeronautics and Space Administration, and (2) NASA's Astrophysics Data System Abstract Service.

REFERENCES

- Abel, N. P., & Satyapal, S., 2008, ApJ, 678, 686
- Alexander, D. M., 2001, MNRAS, 320, 320, L15
- Alexander, T., Sturm, E., Lutz, D., Sternberg, A., Netzer, H., & Genzel, R., 1999, ApJ, 512, 204
- Allen, M. G., Groves, B. A., Dopita, M. A., Sutherland, R. S., Kewley, L. J., 2008, ApJS, 178, 20
- Anscombe, F. J. 1973, American Statistician, 27, 17
- Armus, L., et al., 2007, 656, 148

- Axon, D., 2009, private communication
- Brandl, B. R., et al., 2006, ApJ, 653, 1129, erratum ApJ, 665, 884
- Chiar, J. E., & Tielens, A. G. G. M., 2006, ApJ, 637, 774
- Buchanan, C. L., Gallimore, J. F., O’Dea, C. P., Baum, S. A., Axon, D. J., Robinson, A., Elitzur, M., & Elvis, M., 2006, AJ, 132, 401
- Buchanan, C. L., Gallimore, J. F., O’Dea, C. P., Baum, S. A., Axon, D. J., Robinson, A., Noel-Storr, J., Yzaguirre, A., Elitzur, M., Elvis, M., & Tadhunter, C., 2008, Mem. S. A. It., 75, 282
- Buchanan, C. L., et al., (2009) in preparation.
- Calzetti, D., et al. 2007, ApJ, 666, 870
- Clavel, J., Schulz, B., Altieri, B., Barr, P., Claes, P., Heras, A., Leech, K., Metcalfe, L., & Salama, A., 2000, A&A, 357, 839
- Cleary, K., Lawrence, C. R., Marshall, J. A., Hao, L., & Meier, D., 2007, ApJ, 660, 117
- Dale, D. A., et al., 2006, ApJ, 646, 161
- de Grijp, M. H. K., Keel, W. C., Miley, G. K., Goudfrooij, P., & Lub, J., 1992, A&AS, 96, 389
- Deo, R. P., Crenshaw, D. M., Kraemer, S. B., Dietrich, M., Elitzur, M., Teplitz, H., & Turner, T. J., 2007, ApJ, 671, 124.
- Diamond-Stanic, A. M., Rieke, G. H., & Rigby, J. R., 2009, ApJ, 698, 623
- Draine, B. T., & Li, A., 2007, ApJ, 657, 810
- Draine, B. T., et al., 2007, ApJ, 663, 866
- Dudik, R. P., Weingartner, J. C., Satyapal, S., Fischer, Jacqueline, Dudley, C. C., & O’Halloran, B., 2007, ApJ, 664, 71
- Edelson, R. A., Malkan, M. A., & Rieke, G. H., 1987, ApJ, 321, 233
- Efstathiou, A. & Rowan-Robinson, M., 1995, MNRAS, 273, 649
- Efstathiou, A., 2006, MNRAS, 371, L70

- Farrah, D., et al., 2007, *ApJ*, 667, 149
- Feigelson, E. D., & Nelson, P. I. 1985, *ApJ*, 293, 192
- Finkelstein, D. M. 1986, *Biometrics*, 42, 845
- Galliano, F., 2006, to appear in the proceedings of "Studying Galaxy Evolution with Spitzer and Herschel", astro-ph/0610852
- Galliano, E., Pantin, E., Alloin, D., & Lagage, P. O., 2005, *MNRAS*, 363, L1
- Gallimore, J. F., Yzaguirre, A., Jakoboski, J., Stevenosky, M. J., Axon, D. J., Baum, S. A., Buchannan, C. L., Elitzur, M., Elvis, M., O'Dea, C. P., Robinson, A., 2009, *ApJS*, submitted
- Gallimore, J. F., Buchannan, C. L., Axon, D. J., Baum, S. A., Elitzur, M., Elvis, M., O'Dea, C. P., Robinson, A. X., 2009, in preparation.
- Gebhardt, K., et al. 2000, *ApJ*, 539, L13
- Genzel, R., et al., 1998, *ApJ*, 498, 579
- Granato, G. L. & Danese, L., 1994, *MNRAS*, 268, 235
- Granato, G. L., De Zotti, G., Silva, L., Bressan, A., Danese, L., 2004, *ApJ*, 600, 580
- Groves, B., Dopita, M., & Sutherland, R., 2006, *A&A*, 458, 405
- Gu, Q., Melnick, J., Cid Fernandes, R., Kunth, D., Terlevich, E.; Terlevich, R., 2006, *MNRAS*, 366, 480
- Haas, M., et al., 2003, *A&A*, 402, 87
- Haas, M., Siebenmorgen, R., Schulz, B., Krügel, E., & Chini, R., 2005, *A&A*, 442, L39
- Hao, L., Weedman, D. W., Spoon, H. W. W., Marshall, J. A., Levenson, N. A., Elitzur, M., & Houck, J. R., 2007, *ApJ*, 655, L77
- Hernquist, L. & Mihos, J. C., 1995, *ApJ*, 448, 41
- Ho, L. C., Filippenko, A. V., & Sargent, W. L. W. 1997, *ApJS*, 112, 315
- Houck, J. R., et al. 2004, *ApJS*, 154, 18
- Imanishi, M., Dudley, C. C., Maiolino, R., Maloney, P. R., Nakagawa, T., & Risaliti, G., 2007, *ApJS*, 171, 72

- Isobe, T., Feigelson, E. D., & Nelson, P. I. 1986, *ApJ*, 306, 490
- Kauffmann, G., et al. 2003, *MNRAS*, 346, 1055
- Kendall, M. 1938, *Biometrika*, 30, 81
- Kewley, L. J.; Heisler, C. A.; Dopita, M. A.; Lumsden, S., 2001, *ApJS*, 132, 37
- Kewley, L. J., Groves, B., Kauffmann, G., & Heckman, T., 2006, *MNRAS*, 372, 961
- Kim, D.-C., Sanders, D. B., Veilleux, S., Mazzarella, J. M., Soifer, B. T., 1995, *ApJS*, 98, 129
- Kirhakos, S. D., & Steiner, J. E., 1990, *AJ*, 99, 1722
- Laor, A., & Draine, B. T., 1993, *ApJ*, 402, 441
- Laurent, O., Mirabel, I. F., Charmandaris, V., Gallais, P., Madden, S. C., Sauvage, M., Vigroux, L., & Cesarsky, C., 2000, *A&A*, 359, 887
- Levenson, N. A., Sirocky, M. M., Hao, L., Spoon, H. W. W., Marshall, J. A., Elitzur, M., Houck, J. R., 2007, *ApJ*, 654, L45
- Lu, N., et al., 2008, *PASP*, 120, 328
- Maiolino, R., Ruiz, M., Rieke, G. H., Keller, L. D., 1995, *ApJ*, 446, 561
- Maiolino, R., Shemmer, O., Imanishi, M., Netzer, H., Oliva, E., Lutz, D., & Sturm, E., 2007, *A&A*, 468, 979
- Mason, R. E., Geballe, T. R., Packham, C., Levenson, N. A., Elitzur, M., Fisher, R. S., Perlman, E., 2006, *ApJ*, 640, 612
- Meléndez, M., et al., 2008, *ApJ*, 682, 94
- Merritt, D., & Ferrarese, L. 2001, *ApJ*, 547, 140
- Mihos, J. C., & Hernquist, L., 1996, *ApJ*, 464, 641
- Mor, R., Netzer, H., & Elitzur, M., 2009, *astroph/0907.1654*
- Nenkova, M., Ivezić, Z., & Elitzur, M., 2002, *ApJ*, 570, L9
- Nenkova, M., Sirocky, M. M., Nikutta, R., Ivezić, Z., & Elitzur, M., 2008, *ApJ*, 685, 160
- Netzer, H., et al., 2007, *ApJ*, 666, 806

- Ogle, P., Whysong, D., & Antonucci, R., 2006, *ApJ*, 647, 161
- Packham, C., Radomski, J. T., Roche, P. F., Aitken, D. K., Perlman, E., Alonso-Herrero, A., Colina, L., & Telesco, C. M., 2005, *ApJ*, 618, L17
- Panessa, F. & Bassani, L., 2002, *A&A*, 394, 435
- Peeters, E., Spoon, H. W. W., & Tielens, A. G. G. M., 2004, *ApJ*, 613, 986
- Phillips, M. M. 1979, *ApJ*, 227, L121
- Pier, E. A., & Krolik, J. H., 1992, *ApJ*, 401, 99
- Roussel, H., Sauvage, M., Vigroux, L., & Bosma, A., 2001, *A&A*, 372, 427
- Rush, B., Malkan, M. A., & Spinoglio, L., 1993, *ApJS*, 89, 1
- Schaerer, D., & Stasińska, G., 1999, *A&A*, 345, L17
- Schweitzer, M., et al., 2006, *ApJ*, 649, 79
- Shi, Y., Rieke, G. H., Hines, D. C., Gorjian, V., Werner, M. W., Cleary, K., Low, F. J., Smith, P. S., & Bouwman, J., 2006, *ApJ*, 653, 127
- Shi, Y., Ogle, P., Rieke, G. H., Antonucci, R., Hines, D. C., Smith, P. S., Low, F. J., Bouwman, J., Willmer, C., 2007, *ApJ*, 669, 841
- Shlosman, I., Begelman, M. C., & Frank, J., 1990, *Nature*, 345, 679
- Siebenmorgen, R., Moorwood, A., Freudling, W., & Käeuffl, H. U., 1997, *A&A*, 325, 450
- Siebenmorgen, R., Krügel, E., & Spoon, H. W. W., 2004, *A&A*, 414, 123
- Sirocky, M. M., Levenson, N. A., Elitzur, M., Spoon, H. W. W., & Armus, L., 2008, *ApJ*, 678, 729
- Smith, J. E., Young, S., Robinson, A., Corbett, E. A., Giannuzzo, M. E., Axon, D. J., & Hough, J. H., 2002, *MNRAS*, 335, 773
- Smith, J. D., et al., 2007, *ApJ*, 656, 770
- Smith, J. D., et al., 2007, *PASP*, 119, 1133
- Spinoglio, L., & Malkan, M. A. 1989, *ApJ*, 342, 83
- Spinoglio, L., & Malkan, M. A., *ApJ*, 399, 504

- Spitzer Science Center, 2006, SPICE Spitzer IRS Custom Extraction (Pasadena: SSC)
- Spoon, H. W. W., Marshall, J. A., Houck, J. R., Elitzur, M., Hao, L., Armus, L., Brandl, B. R., & Charmandaris, V., 2007, *ApJ*, 654, L49
- Sprent, P. & Smeeton, N. C. 2000, *Applied Nonparametric Statistical Methods*, (Chapman & Hall/CRC Press: Boca Raton, FL)
- Sturm, E., Lutz, D., Verma, A., Netzer, H., Sternberg, A., Moorwood, A. F. M., Oliva, E., Genzel, R., 2002, *A&A*, 393, 821
- Sturm, E., et al., 2006, *ApJ*, 653, L13
- Sun, J. 1996, *Statistics in Medicine*, 15, 1387
- Thean, A., Pedlar, A., Kukula, M. J., Baum, S. A., O’Dea, C. P., 2001, *MNRAS*, 325, 737
- Tielens, A. G. G. M., Hony, S., van Kerckhoven, C., & Peeters, E., 1999, *The Universe as Seen by ISO*. Eds. P. Cox & M. F. Kessler. ESA-SP 427., p. 579
- Tommasin, S., Spinoglio, L., Malkan, M. A., Smith, H., Charmandaris, V., 2007, *ApJ*, 676, 836
- Tran, H. D. 2003, *ApJ*, 583, 632
- van Bemmell, I. M. & Dullemond, C. P., 2003, *A&A*, 404, 1
- Veilleux, S., Kim, D.-C., Sanders, D. B., Mazzarella, J. M., & Soifer, B. T. 1995, *ApJS*, 98, 171
- Véron-Cetty, M.-P., & Véron, P. 2001, *A&A*, 372, 730
- Véron-Cetty, M.-P., & Véron, P. 2003, *A&A*, 412, 399
- Voit, G. M., 1992a, *MNRAS*, 258, 841
- Voit, G. M., 1992b, *ApJ*, 399, 495
- Weedman, D. W., Hao, L., Higdon, S. J. U., Devost, D., Wu, Y., Charmandaris, V., Brandl, B., Bass, E., & Houck, J. R., 2005, *ApJ*, 633, 706
- Whittle, M., 1992, *ApJS*, 79, 49
- Williams, R. J. R., Baker, A. C., & Perry, J. J., 1999, *MNRAS*, 310, 913

Winkler, H., 1992, MNRAS, 257, 677

Wu, Y., Charmandaris, V., Huang, J., Spinoglio, L., & Tommasin, S., 2009, ApJ, 701, 658

Young, S., Hough, J. H., Efstathiou, A., Wills, B. J., Bailey, J. A., Ward, M. J., & Axon, D. J., 1996, MNRAS, 281, 1206

Table 1. Median Values of Seyfert Properties

Property (1)	Entire Sample (2)	Sy 1.0–1.5, 1n (3)	Sy 1.8–1.9 (4)	Sy 1h, 1i (5)	Sy 2 (6)
Count	83	27	6	17	20
Distance	50.4 ^{83.2} _{22.0}	69.9 ^{107.6} _{34.6}	67.2 ^{107.1} _{21.8}	50.4 ^{77.7} _{26.3}	40.4 ^{67.1} _{32.4}
$\alpha(20 - 30 \mu\text{m})$	-0.76 ^{0.11} _{-1.38}	-1.35 ^{-0.82} _{-1.81}	-0.39 ^{0.10} _{-0.77}	-0.87 ^{-0.52} _{-1.25}	0.16 ^{0.45} _{-0.98}
$\alpha(55 - 90 \mu\text{m})$	-1.31 ^{-0.74} _{-1.81}	-1.54 ^{-1.11} _{-2.03}	-1.05 ^{-0.78} _{-1.28}	-1.69 ^{-1.35} _{-2.61}	-1.24 ^{-0.60} _{-1.53}
$S_\nu(6.7 \mu\text{m})$	0.097 ^{0.163} _{0.038}	0.146 ^{0.186} _{0.094}	0.064 ^{0.209} _{0.013}	0.124 ^{0.265} _{0.060}	0.037 ^{0.082} _{0.023}
$\log \nu L_\nu(6.7 \mu\text{m})$	43.11 ^{43.55} _{42.42}	43.42 ^{43.94} _{43.13}	43.10 ^{43.52} _{42.29}	43.28 ^{43.70} _{42.81}	42.68 ^{43.13} _{42.34}
$\log \nu L_\nu(8.4 \text{ GHz})$	38.04 ^{38.70} _{37.19}	38.40 ^{38.86} _{37.57}	37.87 ^{38.69} _{36.69}	38.37 ^{39.11} _{37.47}	37.75 ^{38.41} _{37.07}
IRAS $\log \nu L_\nu(60 \mu\text{m})$	43.63 ^{43.94} _{43.32}	43.55 ^{43.88} _{43.23}	43.82 ^{44.27} _{43.27}	43.67 ^{43.93} _{43.49}	43.62 ^{44.25} _{43.37}
Sil $10 \mu\text{m}$	0.014 ^{0.137} _{-0.143}	0.117 ^{0.198} _{0.009}	-0.010 ^{0.252} _{-0.169}	-0.120 ^{0.033} _{-0.551}	-0.060 ^{-0.003} _{-0.193}
EW(PAH $6.2 \mu\text{m}$)	184.2 ^{762.9} _{56.9}	84.5 ^{191.1} _{25.5}	615.4 ^{1234.7} _{89.7}	113.8 ^{411.3} _{31.9}	557.0 ^{1547.9} _{190.6}
PAH $6.2 \mu\text{m}$ Flux	112.8 ^{328.8} _{44.2}	69.7 ^{120.0} _{31.9}	127.1 ^{257.6} _{56.9}	161.2 ^{339.0} _{40.4}	183.6 ^{368.8} _{69.6}
$\log L(\text{PAH } 6.2 \mu\text{m})$	41.44 ^{42.08} _{41.09}	41.46 ^{41.63} _{40.98}	41.71 ^{42.22} _{41.25}	41.42 ^{41.94} _{40.85}	41.57 ^{42.32} _{41.20}
EW($\text{H}_2 \text{ S}(1) \lambda 17 \mu\text{m}$)	12.0 ^{42.5} _{1.8}	7.3 ^{20.5} _{1.7}	6.5 ^{8.2} _{2.8}	4.2 ^{18.7} _{0.7}	20.4 ^{47.1} _{7.2}
$\log L(\text{H}_2 \text{ S}(1) \lambda 17 \mu\text{m})$	39.95 ^{40.50} _{39.39}	39.79 ^{40.32} _{39.29}	32.67 ^{40.12} _{6.53}	39.88 ^{40.81} _{38.90}	40.01 ^{40.57} _{39.44}
$\log L(\text{S III } \lambda 18 \mu\text{m})$	40.15 ^{40.69} _{39.70}	40.15 ^{40.59} _{39.39}	40.80 ^{40.94} _{40.27}	40.57 ^{40.67} _{40.00}	40.11 ^{40.93} _{39.88}
EW($\text{Ne V } \lambda 14 \mu\text{m}$)	10.4 ^{17.7} _{2.7}	9.8 ^{15.9} _{1.6}	8.7 ^{10.7} _{6.7}	15.7 ^{28.8} _{6.8}	13.7 ^{17.3} _{7.7}
$\log L(\text{Ne V } \lambda 14 \mu\text{m})$	40.07 ^{40.71} _{38.31}	40.22 ^{40.77} _{38.71}	39.79 ^{40.83} _{24.52}	40.30 ^{41.01} _{40.01}	40.25 ^{40.79} _{39.49}
$\log L(\text{O IV } \lambda 26 \mu\text{m})$	40.65 ^{41.14} _{39.97}	40.71 ^{41.31} _{40.39}	40.73 ^{41.21} _{40.13}	40.97 ^{41.41} _{40.49}	40.63 ^{40.88} _{39.95}
Ne V $14 \mu\text{m} / 24 \mu\text{m}$	0.78 ^{0.93} _{0.62}	0.69 ^{0.86} _{0.60}	0.66 ^{0.79} _{0.58}	0.86 ^{1.08} _{0.81}	0.64 ^{0.77} _{0.60}
S III $18 \mu\text{m} / 33 \mu\text{m}$	0.60 ^{0.72} _{0.47}	0.58 ^{0.68} _{0.40}	0.60 ^{0.79} _{0.57}	0.69 ^{0.73} _{0.55}	0.60 ^{0.69} _{0.40}
PAH $6.2 \mu\text{m} / 11.3 \mu\text{m}$	1.02 ^{1.34} _{0.72}	0.83 ^{1.00} _{0.64}	1.25 ^{1.48} _{0.75}	0.78 ^{1.07} _{0.52}	1.26 ^{1.43} _{0.90}

Note. — Median values of the properties of the 4 subgroups of Seyferts. Col 1. The property. Col 2. Median values for the whole sample. Col 3. Median value for S1 – S1.5, and S1n. Col 4. Median value for S1.8–1.9. Col 5. Median value for S1h and S1i (hidden BLR). Col 6. Median value for S2. Luminosities are reported in ergs s^{-1} , fluxes in $10^{-14} \text{ ergs s}^{-1} \text{ cm}^{-2}$, and EW in nm. Medians were calculated using the Kaplan-Meier estimator where data include lower and upper limits (interval-censored data). Declination limits reduce the sample slightly for the VLA measurements. Several planned MIPS observations never executed, reducing slightly the number of $\alpha(55\text{-}90 \mu\text{m})$ measurements. Non-detections of both lines also affect the sample size for the line ratio measurements.

Table 2. Comparison of Sy 1 and Sy 2 (non-HBLR + HBLR) Properties

Property (1)	n_1 (2)	n_2 (3)	Test Statistic (4)	Value (5)	Two-sided significance (%) (6)
Distance	27	37	KS	0.29	15.8
$\alpha(20 - 30 \mu\text{m})$	27	37	KS	0.42	0.5
$\alpha(55 - 90 \mu\text{m})$	26	36	KS	0.16	75.3
$S_\nu(6.7 \mu\text{m})$	27	37	KS	0.41	0.7
$\log \nu L_\nu(6.7 \mu\text{m})$	27	37	KS	0.35	3.0
IRAS $\log \nu L_\nu(60 \mu\text{m})$	27	37	KS	0.16	82.4
Sil $10 \mu\text{m}$	27	37	KS	0.52	< 0.1
$\log \nu L_\nu(8.4 \text{ GHz})$	24	35	logrank	MC	88.8
EW(PAH $6.2 \mu\text{m}$)	27	37	logrank	MC	0.6
$\log L(\text{PAH } 6.2 \mu\text{m})$	27	37	logrank	MC	75.0
EW($\text{H}_2 \text{ S}(1) \lambda 17 \mu\text{m}$)	27	37	logrank	MC	32.0
$\log L(\text{H}_2 \text{ S}(1) \lambda 17 \mu\text{m})$	27	37	logrank	MC	45.2
$\log L(\text{S III } \lambda 18 \mu\text{m})$	27	37	logrank	MC	14.6
EW($\text{Ne V } \lambda 14 \mu\text{m}$)	27	37	logrank	MC	3.8
$\log L(\text{Ne V } \lambda 14 \mu\text{m})$	27	37	logrank	MC	75.6
$\log L(\text{O IV } \lambda 26 \mu\text{m})$	27	37	logrank	MC	76.4
Ne V $14 \mu\text{m} / 24 \mu\text{m}$	20	26	logrank	MC	16.2
S III $18 \mu\text{m} / 33 \mu\text{m}$	19	28	logrank	MC	64.2
PAH $6.2 \mu\text{m} / 11.3 \mu\text{m}$	26	36	logrank	MC	37.4

Note. — The results of statistical tests to determine if the measured parameters of the Sy 1's and Sy 2's are consistent with being drawn from the same distribution. The samples are defined based on optical classifications: Sy 1 includes S1 – 1.5 and S1n; Sy 2 includes S2, S1h, S1i. Col 1. Property being tested. Col 2. Number of objects in first sample (Sy 1). Col 3. Number of objects in the second sample (Sy 2). Col 4. Type of statistical test: KS is the Kolmogorov-Smirnov test, and logrank is that test from survival analysis, adapted to accommodate lower and upper limits (interval-censored data). Col 5. The value of the test statistic; MC indicates that the probability in Col. 6 was determined by 1000

Monte Carlo trials. Col 6. The probability that the two samples are drawn from the same parent distribution of object properties; low values indicate a significant difference between the samples. Lower limits were removed from the sample of line ratios, but upper limits were included in the analysis.

Table 3. Comparison of Sy 1 and Sy 2 (non-HBLR) Properties

Property (1)	n_1 (2)	n_2 (3)	Test Statistic (4)	Value (5)	Two-sided significance (%) (6)
Distance	27	20	KS	0.32	15.3
$\alpha(20 - 30 \mu\text{m})$	27	20	KS	0.58	< 0.1
$\alpha(55 - 90 \mu\text{m})$	26	19	KS	0.33	13.8
$S_\nu(6.7 \mu\text{m})$	27	20	KS	0.65	< 0.1
$\log \nu L_\nu(6.7 \mu\text{m})$	27	20	KS	0.54	0.1
IRAS $\log \nu L_\nu(60 \mu\text{m})$	27	20	KS	0.23	60.1
Sil $10 \mu\text{m}$	27	20	KS	0.56	< 0.1
$\log \nu L_\nu(8.4 \text{ GHz})$	24	19	logrank	MC	34.4
EW(PAH $6.2 \mu\text{m}$)	27	20	logrank	MC	0.2
$\log L(\text{PAH } 6.2 \mu\text{m})$	27	20	logrank	MC	48.8
EW($\text{H}_2 \text{ S}(1) \lambda 17 \mu\text{m}$)	27	20	logrank	MC	2.2
$\log L(\text{H}_2 \text{ S}(1) \lambda 17 \mu\text{m})$	27	20	logrank	MC	18.8
$\log L(\text{S III } \lambda 18 \mu\text{m})$	27	20	logrank	MC	8.4
EW($\text{Ne V } \lambda 14 \mu\text{m}$)	27	20	logrank	MC	6.0
$\log L(\text{Ne V } \lambda 14 \mu\text{m})$	27	20	logrank	MC	37.8
$\log L(\text{O IV } \lambda 26 \mu\text{m})$	27	20	logrank	MC	70.8
Ne V $14 \mu\text{m} / 24 \mu\text{m}$	20	13	logrank	MC	4.8
S III $18 \mu\text{m} / 33 \mu\text{m}$	19	16	logrank	MC	30.4
PAH $6.2 \mu\text{m} / 11.3 \mu\text{m}$	26	20	logrank	MC	19.8

Note. — The results of statistical tests to determine if the measured parameters of the Sy 1’s and Sy 2’s are consistent with being drawn from the same distribution. The samples are defined based on optical classifications: Sy 1 includes S1–1.5 and S1n; Sy 2 includes S2 only. Col 1. Property being tested. Col 2. Number of objects in first sample (Sy 1). Col 3. Number of objects in the second sample (Sy 2). Col 4. Type of statistical test: KS is the Kolmogorov-Smirnov test, and logrank is that test from survival analysis, adapted to accommodate lower and upper limits (interval-censored data). Col 5. The value of the test statistic. MC indicates that the probability in Col. 6 was determined by 1000 Monte

Carlo trials. Col 6. The probability that the two samples are drawn from the same parent distribution of object properties; low values indicate a significant difference between the samples. Lower limits were removed from the sample of line ratios, but upper limits were included in the analysis.

Table 4. Comparison of HBLR and non-HBLR Sy 2 Properties

Property (1)	n_1 (2)	n_2 (3)	Test Statistic (4)	Value (5)	Two-sided significance (%) (6)
Distance	17	20	KS	0.20	86.8
$\alpha(20 - 30 \mu\text{m})$	17	20	KS	0.59	0.2
$\alpha(55 - 90 \mu\text{m})$	17	19	KS	0.44	4.1
$S_\nu(6.7 \mu\text{m})$	17	20	KS	0.61	0.1
$\log \nu L_\nu(6.7 \mu\text{m})$	17	20	KS	0.46	2.9
IRAS $\log \nu L_\nu(60 \mu\text{m})$	17	20	KS	0.24	58.2
Sil $10 \mu\text{m}$	17	20	KS	0.24	55.4
$\log \nu L_\nu(8.4 \text{ GHz})$	16	19	logrank	MC	8.6
EW(PAH $6.2 \mu\text{m}$)	17	20	logrank	MC	0.4
$\log L(\text{PAH } 6.2 \mu\text{m})$	17	20	logrank	MC	28.4
EW($\text{H}_2 \text{ S}(1) \lambda 17 \mu\text{m}$)	17	20	logrank	MC	0.2
$\log L(\text{H}_2 \text{ S}(1) \lambda 17 \mu\text{m})$	17	20	logrank	MC	16.8
$\log L(\text{S III } \lambda 18 \mu\text{m})$	17	20	logrank	MC	24.8
EW($\text{Ne V } \lambda 14 \mu\text{m}$)	17	20	logrank	MC	76.6
$\log L(\text{Ne V } \lambda 14 \mu\text{m})$	17	20	logrank	MC	6.2
$\log L(\text{O IV } \lambda 26 \mu\text{m})$	17	20	logrank	MC	23.4
Ne V $14 \mu\text{m} / 24 \mu\text{m}$	13	13	logrank	MC	34.6
S III $18 \mu\text{m} / 33 \mu\text{m}$	12	16	logrank	MC	18.8
PAH $6.2 \mu\text{m} / 11.3 \mu\text{m}$	16	20	logrank	MC	6.6

Note. — The results of statistical tests to determine if the measured parameters of hidden Sy 1’s and standard Sy 2’s are consistent with being drawn from the same distribution. The samples are defined based on optical classifications, with HBLR comprising S1i and S1h, and non-HBLR comprising only S2. Col 1. Property being tested. Col 2. Number of objects in first sample (Sy 1). Col 3. Number of objects in the second sample (Sy 2). Col 4. Type of statistical test: KS is the Kolmogorov-Smirnov test, and logrank is that test from survival analysis, adapted to accommodate lower and upper limits (interval-censored data). Col 5. The value of the test statistic. MC indicates that the probability in Col. 6 was determined

by 1000 Monte Carlo trials. Col 6. The probability that the two samples are drawn from the same parent distribution of object properties; low values indicate a significant difference between the samples. Lower limits were removed from the sample of line ratios, but upper limits were included in the analysis.

Table 5. Comparison of Sy 1 and HBLR Sy 2 Properties

Property (1)	n_1 (2)	n_2 (3)	Test Statistic (4)	Value (5)	Two-sided significance (%) (6)
Distance	27	17	KS	0.26	47.4
$\alpha(20 - 30 \mu\text{m})$	27	17	KS	0.37	8.2
$\alpha(55 - 90 \mu\text{m})$	26	17	KS	0.19	76.6
$S_\nu(6.7 \mu\text{m})$	27	17	KS	0.22	61.7
$\log \nu L_\nu(6.7 \mu\text{m})$	27	17	KS	0.31	20.9
IRAS $\log \nu L_\nu(60 \mu\text{m})$	27	17	KS	0.22	67.0
Sil $10 \mu\text{m}$	27	17	KS	0.51	0.8
$\log \nu L_\nu(8.4 \text{ GHz})$	24	16	logrank	MC	24.8
EW(PAH $6.2 \mu\text{m}$)	27	17	logrank	MC	70.8
$\log L(\text{PAH } 6.2 \mu\text{m})$	27	17	logrank	MC	95.4
EW($\text{H}_2 \text{ S}(1) \lambda 17 \mu\text{m}$)	27	17	logrank	MC	32.6
$\log L(\text{H}_2 \text{ S}(1) \lambda 17 \mu\text{m})$	27	17	logrank	MC	61.2
$\log L(\text{S III } \lambda 18 \mu\text{m})$	27	17	logrank	MC	60.6
EW($\text{Ne V } \lambda 14 \mu\text{m}$)	27	17	logrank	MC	20.0
$\log L(\text{Ne V } \lambda 14 \mu\text{m})$	27	17	logrank	MC	18.4
$\log L(\text{O IV } \lambda 26 \mu\text{m})$	27	17	logrank	MC	26.8
Ne V $14 \mu\text{m} / 24 \mu\text{m}$	20	13	logrank	MC	72.8
S III $18 \mu\text{m} / 33 \mu\text{m}$	19	12	logrank	MC	66.8
PAH $6.2 \mu\text{m} / 11.3 \mu\text{m}$	26	16	logrank	MC	90.2

Note. — The results of statistical tests to determine if the measured parameters of Sy 1’s and Sy 2’s with HBLR are consistent with being drawn from the same distribution. The samples are defined based on optical classifications. Col 1. Property being tested. Col 2. Number of objects in first sample (Sy 1). Col 3. Number of objects in the second sample (Sy 2). Col 4. Type of statistical test: KS is the Kolmogorov-Smirnov test, and logrank is that test from survival analysis, adapted to accommodate lower and upper limits (interval-censored data). Col 5. The value of the test statistic. MC indicates that the probability

in Col. 6 was determined by 1000 Monte Carlo trials. Col 6. The probability that the two samples are drawn from the same parent distribution of object properties; low values indicate a significant difference between the samples. Lower limits were removed from the sample of line ratios, but upper limits were included in the analysis.

Table 6. Comparison of Sy 1.8–1.9 and non-HBLR Sy 2 Properties

Property (1)	n_1 (2)	n_2 (3)	Test Statistic (4)	Value (5)	Two-sided significance (%) (6)
Distance	6	20	KS	0.35	52.8
$\alpha(20 - 30 \mu\text{m})$	6	20	KS	0.38	40.9
$\alpha(55 - 90 \mu\text{m})$	6	19	KS	0.26	82.2
$S_\nu(6.7 \mu\text{m})$	6	20	KS	0.33	59.3
$\log \nu L_\nu(6.7 \mu\text{m})$	6	20	KS	0.35	52.8
IRAS $\log \nu L_\nu(60 \mu\text{m})$	6	20	KS	0.20	97.2
Sil $10 \mu\text{m}$	6	20	KS	0.33	59.3
$\log \nu L_\nu(8.4 \text{ GHz})$	6	19	logrank	MC	68.6
EW(PAH $6.2 \mu\text{m}$)	6	20	logrank	MC	59.4
$\log L(\text{PAH } 6.2 \mu\text{m})$	6	20	logrank	MC	91.2
EW($\text{H}_2 \text{ S}(1) \lambda 17 \mu\text{m}$)	6	20	logrank	MC	31.6
$\log L(\text{H}_2 \text{ S}(1) \lambda 17 \mu\text{m})$	6	20	logrank	MC	25.2
$\log L(\text{S III } \lambda 18 \mu\text{m})$	6	20	logrank	MC	32.2
EW($\text{Ne V } \lambda 14 \mu\text{m}$)	6	20	logrank	MC	38.2
$\log L(\text{Ne V } \lambda 14 \mu\text{m})$	6	20	logrank	MC	49.2
$\log L(\text{O IV } \lambda 26 \mu\text{m})$	6	20	logrank	MC	72.6
Ne V $14 \mu\text{m} / 24 \mu\text{m}$	4	13	KS	0.29	91.9
S III $18 \mu\text{m} / 33 \mu\text{m}$	5	16	logrank	MC	13.2
PAH $6.2 \mu\text{m} / 11.3 \mu\text{m}$	6	20	logrank	MC	37.6

Note. — The results of statistical tests to determine if the measured parameters of Sy 1.8–1.9 and Sy 2’s without HBLR are consistent with being drawn from the same distribution. The samples are defined based on optical classifications. Col 1. Property being tested. Col 2. Number of objects in first sample (Sy 1). Col 3. Number of objects in the second sample (Sy 2). Col 4. Type of statistical test: KS is the Kolmogorov-Smirnov test, and logrank is that test from survival analysis, adapted to accommodate lower and upper limits (interval-censored data). Col 5. The value of the test statistic. MC indicates that the probability in Col. 6 was determined by 1000 Monte Carlo trials. Col 6. The probability that the two

samples are drawn from the same parent distribution of object properties; low values indicate a significant difference between the samples. Lower limits were removed from the sample of line ratios, but upper limits were included in the analysis.

Table 7. Comparison of Sy 1.8–1.9 and HBLR Sy 2 Properties

Property (1)	n_1 (2)	n_2 (3)	Test Statistic (4)	Value (5)	Two-sided significance (%) (6)
Distance	6	17	KS	0.26	84.7
$\alpha(20 - 30 \mu\text{m})$	6	17	KS	0.44	25.0
$\alpha(55 - 90 \mu\text{m})$	6	17	KS	0.66	2.4
$S_\nu(6.7 \mu\text{m})$	6	17	KS	0.44	25.0
$\log \nu L_\nu(6.7 \mu\text{m})$	6	17	KS	0.27	79.3
IRAS $\log \nu L_\nu(60 \mu\text{m})$	6	17	KS	0.44	25.0
Sil $10 \mu\text{m}$	6	17	KS	0.35	54.1
$\log \nu L_\nu(8.4 \text{ GHz})$	6	16	logrank	MC	17.6
EW(PAH $6.2 \mu\text{m}$)	6	17	logrank	MC	3.2
$\log L(\text{PAH } 6.2 \mu\text{m})$	6	17	logrank	MC	54.4
EW($\text{H}_2 \text{ S}(1) \lambda 17 \mu\text{m}$)	6	17	logrank	MC	7.4
$\log L(\text{H}_2 \text{ S}(1) \lambda 17 \mu\text{m})$	6	17	logrank	MC	81.2
$\log L(\text{S III } \lambda 18 \mu\text{m})$	6	17	logrank	MC	67.4
EW($\text{Ne V } \lambda 14 \mu\text{m}$)	6	17	logrank	MC	72.0
$\log L(\text{Ne V } \lambda 14 \mu\text{m})$	6	17	logrank	MC	38.2
$\log L(\text{O IV } \lambda 26 \mu\text{m})$	6	17	logrank	MC	44.8
Ne V $14 \mu\text{m} / 24 \mu\text{m}$	4	13	logrank	MC	38.8
S III $18 \mu\text{m} / 33 \mu\text{m}$	5	12	logrank	MC	39.0
PAH $6.2 \mu\text{m} / 11.3 \mu\text{m}$	6	16	logrank	MC	3.4

Note. — The results of statistical tests to determine if the measured parameters of Sy 1.8-1.9 and Sy 2’s with HBLR are consistent with being drawn from the same distribution. The samples are defined based on optical classifications. Col 1. Property being tested. Col 2. Number of objects in first sample (Sy 1). Col 3. Number of objects in the second sample (Sy 2). Col 4. Type of statistical test: KS is the Kolmogorov-Smirnov test, and logrank is that test from survival analysis, adapted to accommodate lower and upper limits (interval-censored data). Col 5. The value of the test statistic. MC indicates that the probability in Col. 6 was determined by 1000 Monte Carlo trials. Col 6. The probability that the two

samples are drawn from the same parent distribution of object properties; low values indicate a significant difference between the samples. Lower limits were removed from the sample of line ratios, but upper limits were included in the analysis.

Table 8. Comparison of Sy 1.8–1.9 and Sy 1 Properties

Property (1)	n_1 (2)	n_2 (3)	Test Statistic (4)	Value (5)	Two-sided significance (%) (6)
Distance	6	27	KS	0.17	99.6
$\alpha(20 - 30 \mu\text{m})$	6	27	KS	0.65	1.8
$\alpha(55 - 90 \mu\text{m})$	6	26	KS	0.54	7.9
$S_\nu(6.7 \mu\text{m})$	6	27	KS	0.46	18.5
$\log \nu L_\nu(6.7 \mu\text{m})$	6	27	KS	0.31	62.2
IRAS $\log \nu L_\nu(60 \mu\text{m})$	6	27	KS	0.39	44.8
Sil $10 \mu\text{m}$	6	27	KS	0.43	26.6
$\log \nu L_\nu(8.4 \text{ GHz})$	6	24	logrank	MC	16.8
EW(PAH $6.2 \mu\text{m}$)	6	27	logrank	MC	1.2
$\log L(\text{PAH } 6.2 \mu\text{m})$	6	27	logrank	MC	59.8
EW($\text{H}_2 \text{ S}(1) \lambda 17 \mu\text{m}$)	6	27	logrank	MC	30.4
$\log L(\text{H}_2 \text{ S}(1) \lambda 17 \mu\text{m})$	6	27	logrank	MC	57.0
$\log L(\text{S III } \lambda 18 \mu\text{m})$	6	27	logrank	MC	95.0
EW($\text{Ne V } \lambda 14 \mu\text{m}$)	6	27	logrank	MC	39.6
$\log L(\text{Ne V } \lambda 14 \mu\text{m})$	6	27	logrank	MC	84.4
$\log L(\text{O IV } \lambda 26 \mu\text{m})$	6	27	logrank	MC	65.6
Ne V $14 \mu\text{m} / 24 \mu\text{m}$	4	20	logrank	MC	48.8
S III $18 \mu\text{m} / 33 \mu\text{m}$	5	19	logrank	MC	35.2
PAH $6.2 \mu\text{m} / 11.3 \mu\text{m}$	6	26	logrank	MC	20.4

Note. — The results of statistical tests to determine if the measured parameters of Sy 1.8–1.9 and Sy 1’s are consistent with being drawn from the same distribution. The samples are defined based on optical classifications. Col 1. Property being tested. Col 2. Number of objects in first sample (Sy 1). Col 3. Number of objects in the second sample (Sy 2). Col 4. Type of statistical test: KS is the Kolmogorov-Smirnov test, and logrank is that test from survival analysis, adapted to accommodate lower and upper limits (interval-censored data). Col 5. The value of the test statistic. MC indicates that the probability in Col. 6 was determined by 1000 Monte Carlo trials. Col 6. The probability that the two samples are

drawn from the same parent distribution of object properties; low values indicate a significant difference between the samples. Lower limits were removed from the sample of line ratios, but upper limits were included in the analysis.

Table 9. Comparison of (Sy 1 + HBLR Sy 2) and (Sy 1.8–1.9 + non-HBLR Sy 2) Properties

Property (1)	n_1 (2)	n_2 (3)	Test Statistic (4)	Value (5)	Two-sided significance (%) (6)
Distance	44	26	KS	0.18	65.2
$\alpha(20 - 30 \mu\text{m})$	44	26	KS	0.55	< 0.1
$\alpha(55 - 90 \mu\text{m})$	43	25	KS	0.39	1.1
$S_\nu(6.7 \mu\text{m})$	44	26	KS	0.55	< 0.1
$\log \nu L_\nu(6.7 \mu\text{m})$	44	26	KS	0.44	0.2
IRAS $\log \nu L_\nu(60 \mu\text{m})$	44	26	KS	0.26	23.7
Sil $10 \mu\text{m}$	44	26	KS	0.35	3.5
$\log \nu L_\nu(8.4 \text{ GHz})$	40	25	logrank	MC	5.6
EW(PAH $6.2 \mu\text{m}$)	44	26	logrank	MC	0.2
$\log L(\text{PAH } 6.2 \mu\text{m})$	44	26	logrank	MC	28.2
EW($\text{H}_2 \text{ S}(1) \lambda 17 \mu\text{m}$)	44	26	logrank	MC	0.6
$\log L(\text{H}_2 \text{ S}(1) \lambda 17 \mu\text{m})$	44	26	logrank	MC	19.6
$\log L(\text{S III } \lambda 18 \mu\text{m})$	44	26	logrank	MC	14.4
EW($\text{Ne V } \lambda 14 \mu\text{m}$)	44	26	logrank	MC	28.4
$\log L(\text{Ne V } \lambda 14 \mu\text{m})$	44	26	logrank	MC	13.2
$\log L(\text{O IV } \lambda 26 \mu\text{m})$	44	26	logrank	MC	34.0
Ne V $14 \mu\text{m} / 24 \mu\text{m}$	33	17	logrank	MC	8.2
S III $18 \mu\text{m} / 33 \mu\text{m}$	31	21	logrank	MC	42.0
PAH $6.2 \mu\text{m} / 11.3 \mu\text{m}$	42	26	logrank	MC	3.8

Note. — The results of statistical tests to determine if the measured parameters of the combined groups (Sy 1 + HBLR Sy 2) and (Sy 1.8–1.9 and non-HBLR Sy 2) are consistent with being drawn from the same distribution. The samples are defined based on optical classifications. Col 1. Property being tested. Col 2. Number of objects in first sample (Sy 1). Col 3. Number of objects in the second sample (Sy 2). Col 4. Type of statistical test: KS is the Kolmogorov-Smirnov test, and logrank is that test from survival analysis,

adapted to accommodate lower and upper limits (interval-censored data). Col 5. The value of the test statistic. MC indicates that the probability in Col. 6 was determined by 1000 Monte Carlo trials. Col 6. The probability that the two samples are drawn from the same parent distribution of object properties; low values indicate a significant difference between the samples. Lower limits were removed from the sample of line ratios, but upper limits were included in the analysis.

Table 10. Tests for Correlations in Seyfert Properties

First Property (1)	Second Property (2)	z (3)	$p(\%)$ (4)
EW(PAH 6.2 μm)	Distance	-2.058	4.0
EW(PAH 6.2 μm)	Sil 10 μm	-2.311	2.1
EW(PAH 6.2 μm)	$\alpha(20 - 30 \mu\text{m})$	7.691	< 0.1
EW(PAH 6.2 μm)	$\alpha(55 - 90 \mu\text{m})$	5.663	< 0.1
EW(PAH 6.2 μm)	EW(H ₂ S(1) $\lambda 17\mu\text{m}$)	4.888	< 0.1
EW(PAH 6.2 μm)	EW(Ne V $\lambda 14 \mu\text{m}$)	2.220	2.6
EW(PAH 6.2 μm)	$\log L(\text{Ne V } \lambda 14 \mu\text{m})$	-0.668	50.4
PAH 6.2 μm Flux	Ne V $\lambda 14 \mu\text{m}$ Flux	1.933	5.3
$\log L(\text{PAH } 6.2 \mu\text{m})$	$\log L(\text{Ne V } \lambda 14 \mu\text{m})$	4.205	< 0.1
PAH 6.2 μm Flux	H ₂ S(1) $\lambda 17\mu\text{m}$ Flux	4.969	< 0.1
$\log L(\text{PAH } 6.2 \mu\text{m})$	$\log L(\text{H}_2 \text{ S}(1) \lambda 17\mu\text{m})$	5.333	< 0.1
$\log L(\text{PAH } 6.2 \mu\text{m})$	$\alpha(20 - 30 \mu\text{m})$	2.671	0.8
$\log L(\text{PAH } 6.2 \mu\text{m})$	$\alpha(55 - 90 \mu\text{m})$	1.370	17.1
PAH 6.2 μm Flux	IRAS $S_\nu(60 \mu\text{m})$	7.260	< 0.1
$\log L(\text{PAH } 6.2 \mu\text{m})$	IRAS $\log \nu L_\nu(60 \mu\text{m})$	7.491	< 0.1
PAH 6.2 μm Flux	O IV $\lambda 26 \mu\text{m}$ Flux	1.029	30.3
$\log L(\text{PAH } 6.2 \mu\text{m})$	$\log L(\text{O IV } \lambda 26 \mu\text{m})$	2.744	0.6
$\alpha(20 - 30 \mu\text{m})$	$\alpha(55 - 90 \mu\text{m})$	4.288	< 0.1
$\alpha(20 - 30 \mu\text{m})$	EW(H ₂ S(1) $\lambda 17\mu\text{m}$)	4.292	< 0.1
$\alpha(20 - 30 \mu\text{m})$	IRAS $\log \nu L_\nu(60 \mu\text{m})$	2.788	0.5
$\alpha(20 - 30 \mu\text{m})$	EW(Ne V $\lambda 14 \mu\text{m}$)	2.933	0.3
$\alpha(20 - 30 \mu\text{m})$	$\log L(\text{Ne V } \lambda 14 \mu\text{m})$	-0.317	75.2
$\alpha(20 - 30 \mu\text{m})$	$\log L(\text{S III } \lambda 18 \mu\text{m})$	2.861	0.4
$\alpha(20 - 30 \mu\text{m})$	Sil 10 μm	-4.674	< 0.1
$S_\nu(6.7 \mu\text{m})$	Ne V $\lambda 14 \mu\text{m}$ Flux	3.228	0.1
$\log \nu L_\nu(6.7 \mu\text{m})$	$\log L(\text{Ne V } \lambda 14 \mu\text{m})$	5.136	< 0.1
$S_\nu(6.7 \mu\text{m})$	PAH 6.2 μm Flux	-0.690	49.0
$\log \nu L_\nu(6.7 \mu\text{m})$	$\log L(\text{PAH } 6.2 \mu\text{m})$	2.884	0.4
EW(Ne V $\lambda 14 \mu\text{m}$)	Sil 10 μm	-2.997	0.3
Ne V $\lambda 14 \mu\text{m}$ Flux	$S_\nu(8.4 \text{ GHz})$	3.118	0.2

Table 10—Continued

First Property (1)	Second Property (2)	z (3)	p (%) (4)
$\log L(\text{Ne V } \lambda 14 \mu\text{m})$	$\log \nu L_\nu(8.4 \text{ GHz})$	4.371	< 0.1
Ne V $\lambda 14 \mu\text{m}$ Flux	IRAS $S_\nu(60 \mu\text{m})$	2.724	0.6
$\log L(\text{Ne V } \lambda 14 \mu\text{m})$	IRAS $\log \nu L_\nu(60 \mu\text{m})$	4.808	< 0.1
$\log L(\text{Ne V } \lambda 14 \mu\text{m})$	Sil $10 \mu\text{m}$	−0.410	68.1
Ne V $14 \mu\text{m} / 24 \mu\text{m}$	S III $18 \mu\text{m} / 33 \mu\text{m}$	−0.171	86.4
Ne V $14 \mu\text{m} / 24 \mu\text{m}$	Sil $10 \mu\text{m}$	−0.914	36.1
PAH $6.2 \mu\text{m} / 11.3 \mu\text{m}$	$\log L(\text{Ne V } \lambda 14 \mu\text{m})$	0.501	61.7
PAH $6.2 \mu\text{m} / 11.3 \mu\text{m}$	Sil $10 \mu\text{m}$	−0.006	99.5
X-ray Flux (2–10 keV)	Ne V $\lambda 14 \mu\text{m}$ Flux	1.685	9.2
O III Flux	Ne V $\lambda 14 \mu\text{m}$ Flux	1.811	7.0
Ne V $14 \mu\text{m} / [\text{NeII}]$	EW(PAH $6.2 \mu\text{m}$)	−5.261	< 0.1
O III / Ne V ($14 \mu\text{m}$)	Sil $10 \mu\text{m}$	4.197	< 0.1
O III / O IV ($26 \mu\text{m}$)	Sil $10 \mu\text{m}$	4.121	< 0.1
$\log L(\text{O IV } \lambda 26 \mu\text{m})$	$\log L(\text{O III})$	4.847	< 0.1
O IV $\lambda 26 \mu\text{m}$ Flux	O III Flux	2.564	1.0
$\log L(\text{Ne V } \lambda 14 \mu\text{m})$	$\log L(\text{O III})$	4.655	< 0.1
Ne V $\lambda 14 \mu\text{m}$ Flux	O III Flux	1.811	7.0
$\log L(\text{Ne V } \lambda 14 \mu\text{m})$	Sil $10 \mu\text{m}$	−0.410	68.1
N_{H} (cm^{-2})	Sil $10 \mu\text{m}$	−2.372	1.8

Note. — The results of non-parametric rank tests to look for correlations among the properties of the combined sample. Col 1 & 2. Properties tested for correlation. Col 3. Kendall’s generalized rank correlation coefficient, adjusted to account for upper and lower limits. Reported is the z -score, following the method outlined by Isobe, Feigelson, & Nelson (1986). Col 4. Two-sided significance, giving the probability of no correlation; small values ($p < 1\%$) indicate evidence for correlation.

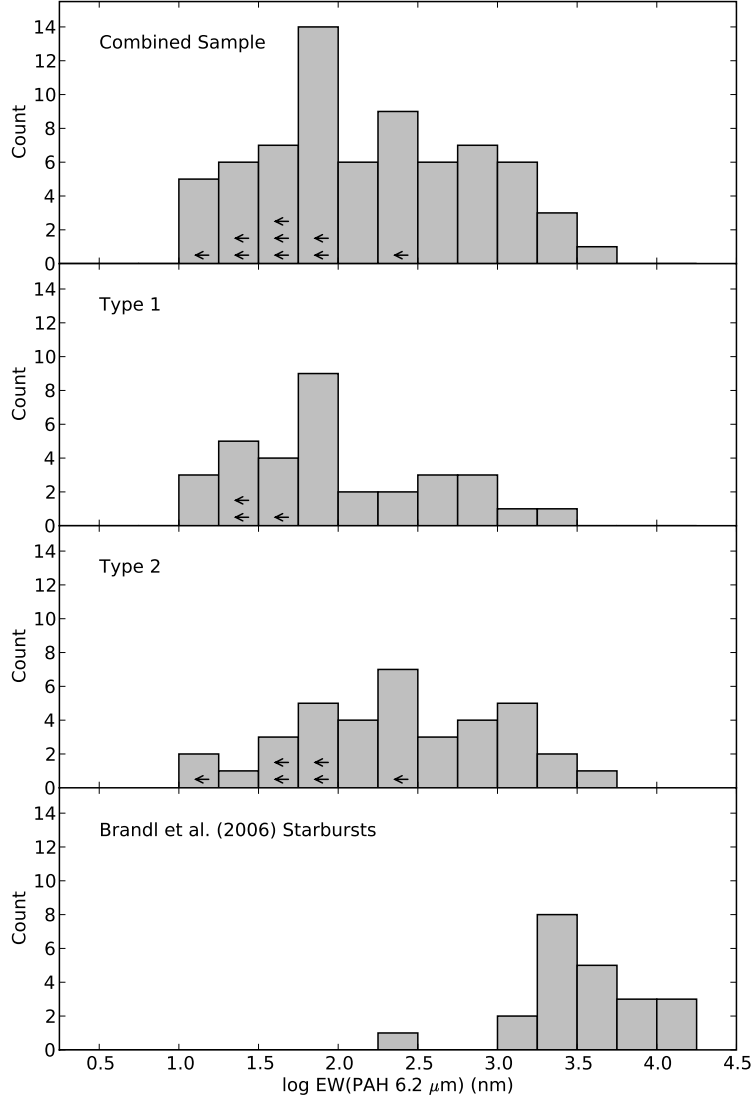


Fig. 1.— The distribution of $6.2 \mu\text{m}$ PAH EW. From the top, the panels are (1) Sy 1 and Sy 2; (2) Sy 1 (S1.0–1.9, S1n), (3) Sy 2 (S2, S1h, & S1i), and starbursts from the Brandl et al. (2006) sample. Note that the Brandl et al. sample shares two objects in common with our sample, NGC 1097 and NGC1365. The starburst measurements are derived from a PAHFIT spectral decomposition of the Brandl et al. data.

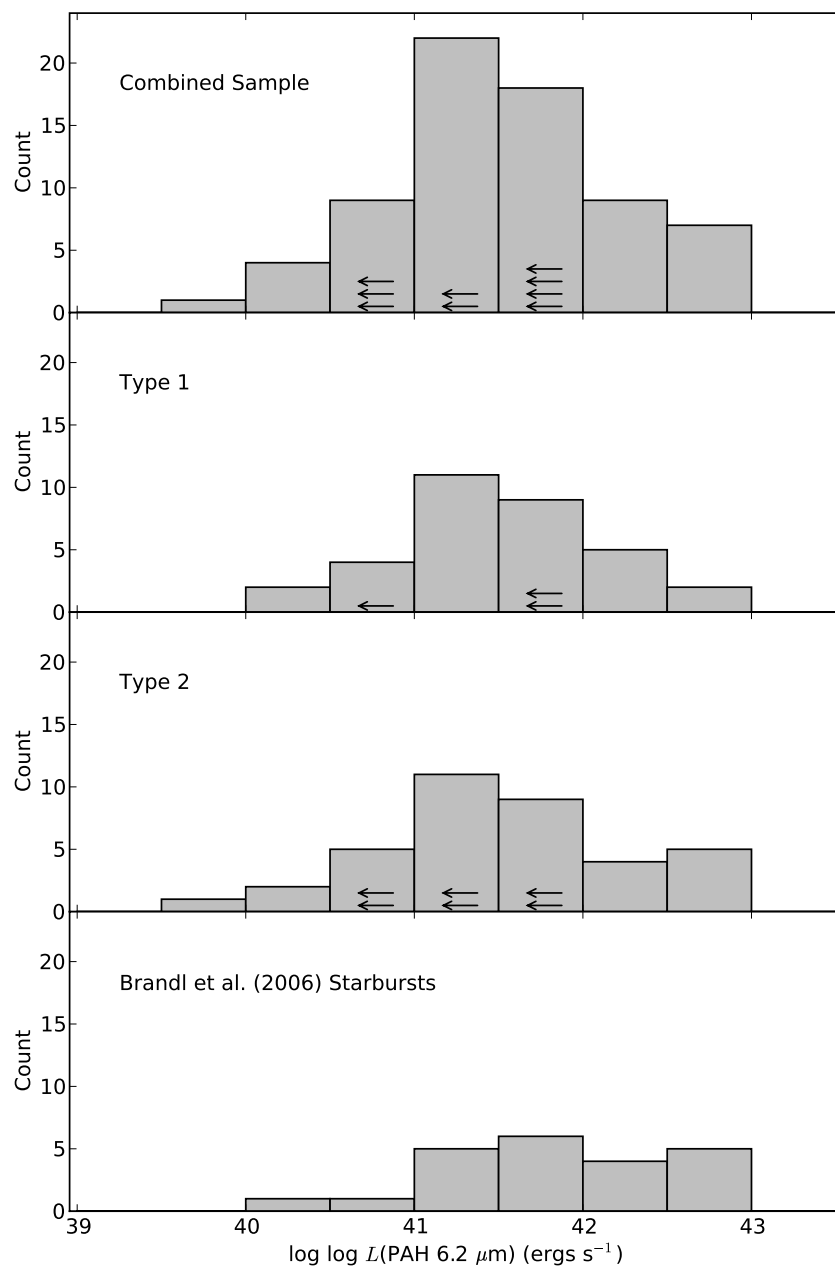


Fig. 2.— The distribution of $6.2 \mu\text{m}$ PAH luminosity. From the top, the panels are (1) Sy 1 and Sy 2; (2) Sy 1 (S1.0–1.9, S1n), (3) Sy 2 (S1, S1h, & S1i), and starbursts from the Brandl et al. (2006) sample. Note that the Brandl et al. sample shares two objects in common with our sample, NGC 1097 and NGC1365. The starburst measurements are derived from a PAHFIT spectral decomposition of the Brandl et al. data.

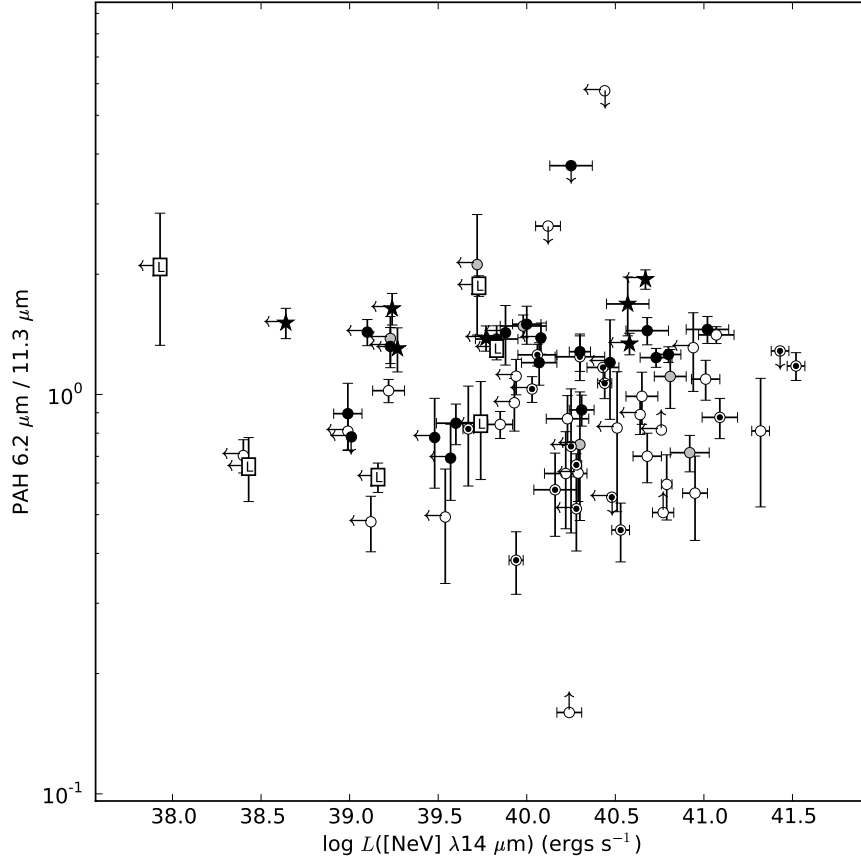


Fig. 3.— The ratio of 6.2/11.3 μm PAH strength as a function of [NeV] luminosity. Open circles are S1, S1.5, and S1n, gray-filled circles are S1.8 and S1.9, filled circles are Sy 2, partially filled circles are “hidden Seyferts” (S1h and S1i), squares labeled L are LINERs, and filled stars are Starburst/HII galaxies. Limits are indicated by appropriately directed arrows. The single lower limit in the PAH ratio is MRK 704, for which the 11.3 μm feature is not detected.

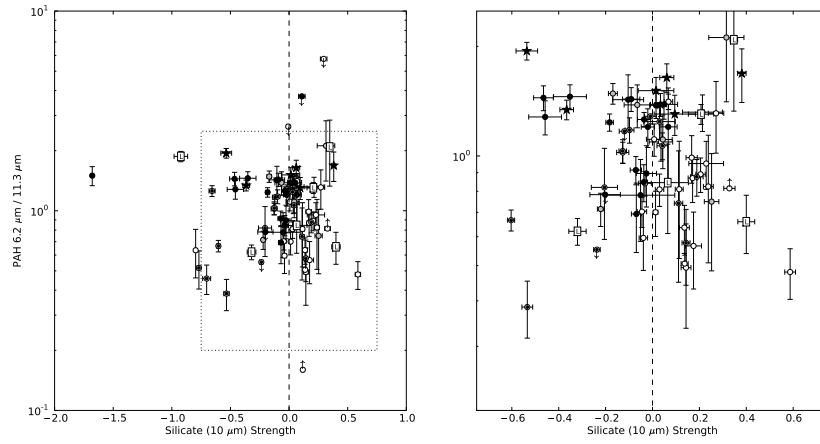


Fig. 4.— Ratio of the 6.2 and 11.3 μm PAH lines vs. Sil 10 μm strength. For the Sil 10 μm strength, positive means emission. (Left) the data. (Right) a blow up of the region around a Sil strength of zero. Open circles are S1, S1.5, and S1n, gray-filled circles are S1.8 and S1.9, filled circles are Sy 2, partially filled circles are “hidden Seyferts” (S1h and S1i), squares labeled L are LINERs, and filled stars are Starburst/HII galaxies. Limits are indicated by appropriately directed arrows.

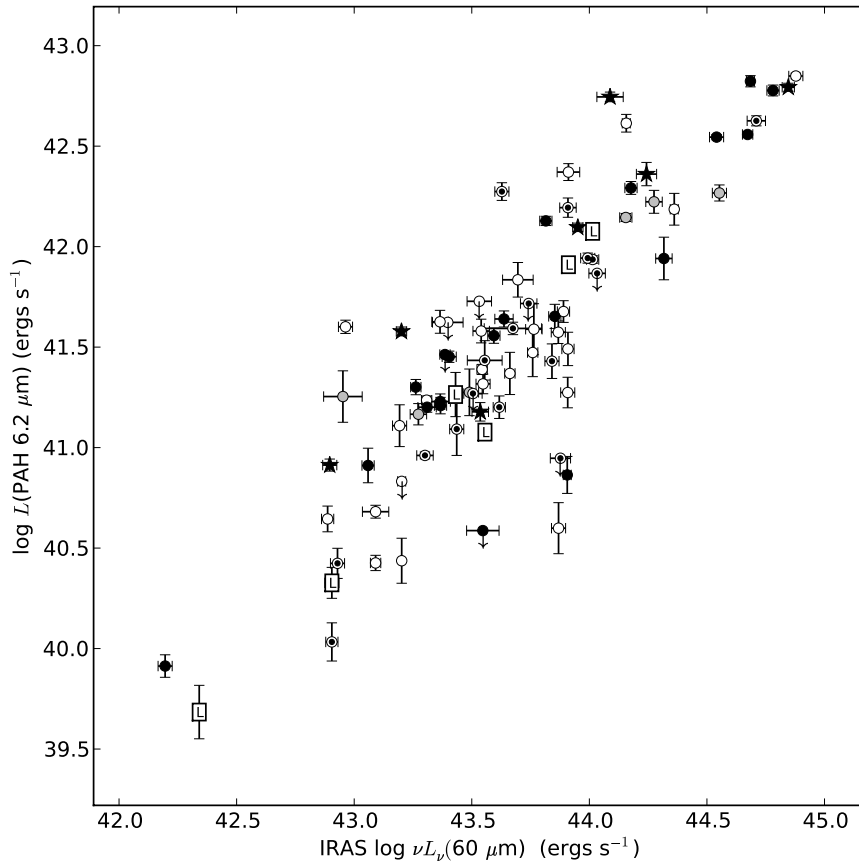


Fig. 5.— $6.2 \mu\text{m}$ PAH luminosity vs. IRAS $\nu L_\nu(60 \mu\text{m})$. Open circles are S1, S1.5, and S1n, gray-filled circles are S1.8 and S1.9, filled circles are Sy 2, partially filled circles are “hidden Seyferts” (S1h and S1i), squares labeled L are LINERs, and filled stars are Starburst/HII galaxies.

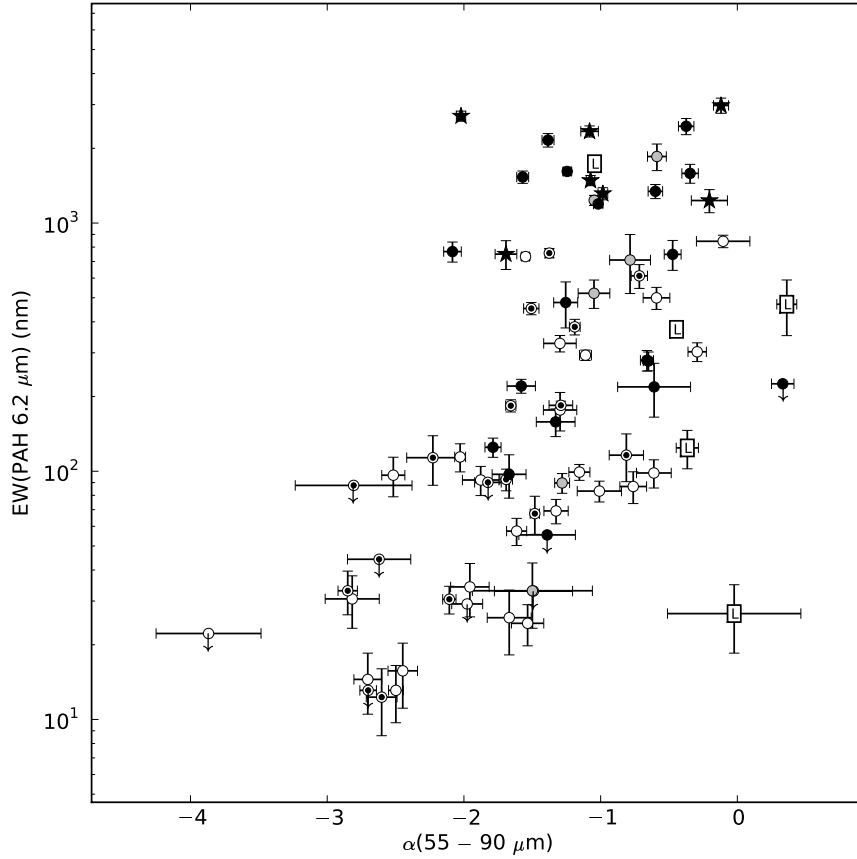


Fig. 6.— 6.2 μm PAH EW vs. slope of the MIPS SED. The slope of the MIPS SED indicates the relative importance of cold vs. warm dust to the FIR SED. Positive slope is a red MFIR SED. Open circles are S1, S1.5, and S1n, gray-filled circles are S1.8 and S1.9, filled circles are Sy 2, partially filled circles are “hidden Seyferts” (S1h and S1i), squares labeled L are LINERs, and filled stars are Starburst/HII galaxies.

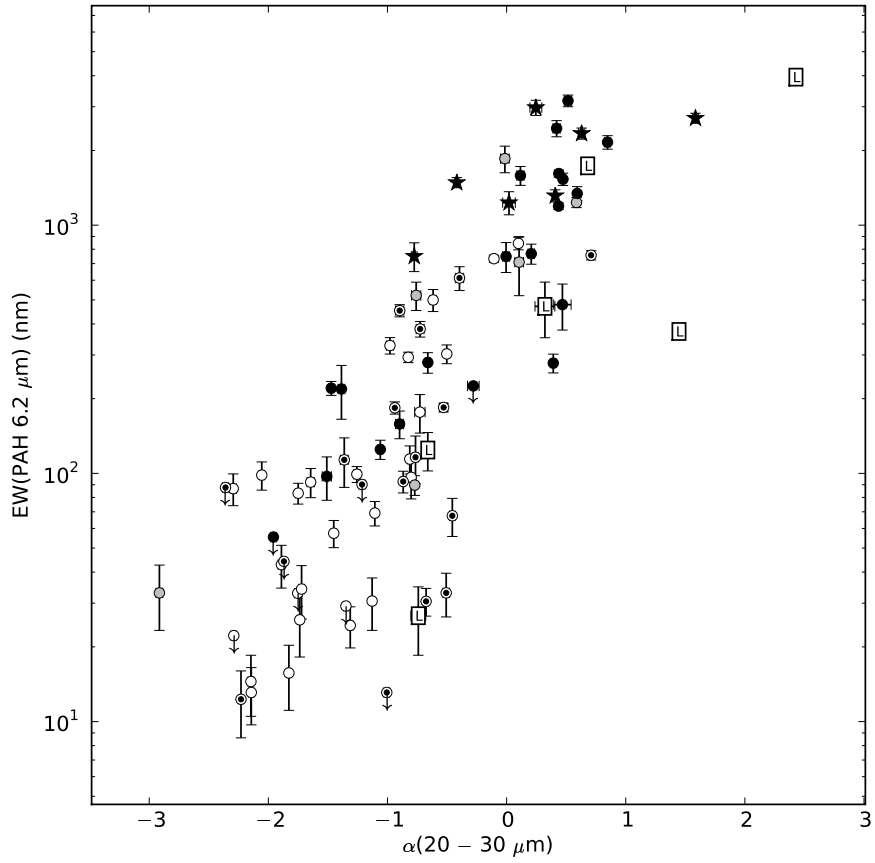


Fig. 7.— 6.2 μm PAH EW vs. spectral index of the continuum between 20 and 30 μm . Positive slope is a red MFIR SED. Open circles are S1, S1.5, and S1n, gray-filled circles are S1.8 and S1.9, filled circles are Sy 2, partially filled circles are “hidden Seyferts” (S1h and S1i), squares labeled L are LINERs, and filled stars are Starburst/HII galaxies.

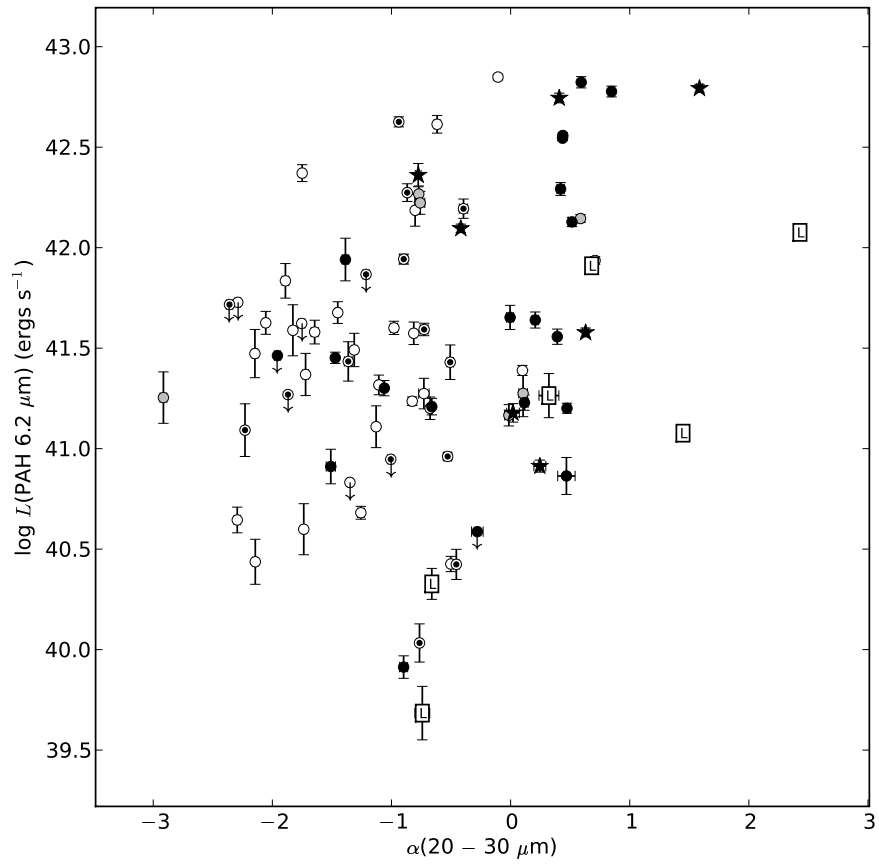


Fig. 8.— Luminosity of the PAH 6.2 μm feature vs. spectral index of the continuum between 20 and 30 μm . Open circles are S1, S1.5, and S1n, gray-filled circles are S1.8 and S1.9, filled circles are Sy 2, partially filled circles are “hidden Seyferts” (S1h and S1i), squares labeled L are LINERs, and filled stars are Starburst/HII galaxies.

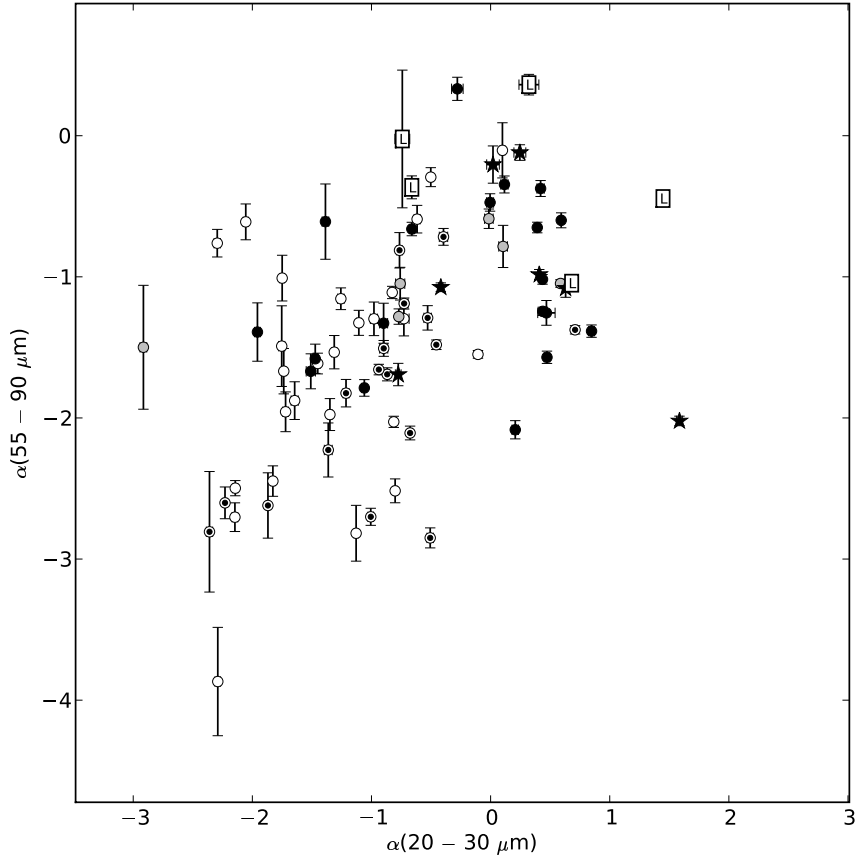


Fig. 9.— MIPS SED slope vs. IRS 20-30 μm spectral index. Sources with blue or flat MIPS SEDs tend to have flat 20-30 SEDs. Sources with red MIPS SEDs tend to have red 20-30 SEDs with a broad distribution. Open circles are S1, S1.5, and S1n, gray-filled circles are S1.8 and S1.9, filled circles are Sy 2, partially filled circles are “hidden Seyferts” (S1h and S1i), squares labeled L are LINERs, and filled stars are Starburst/HII galaxies.

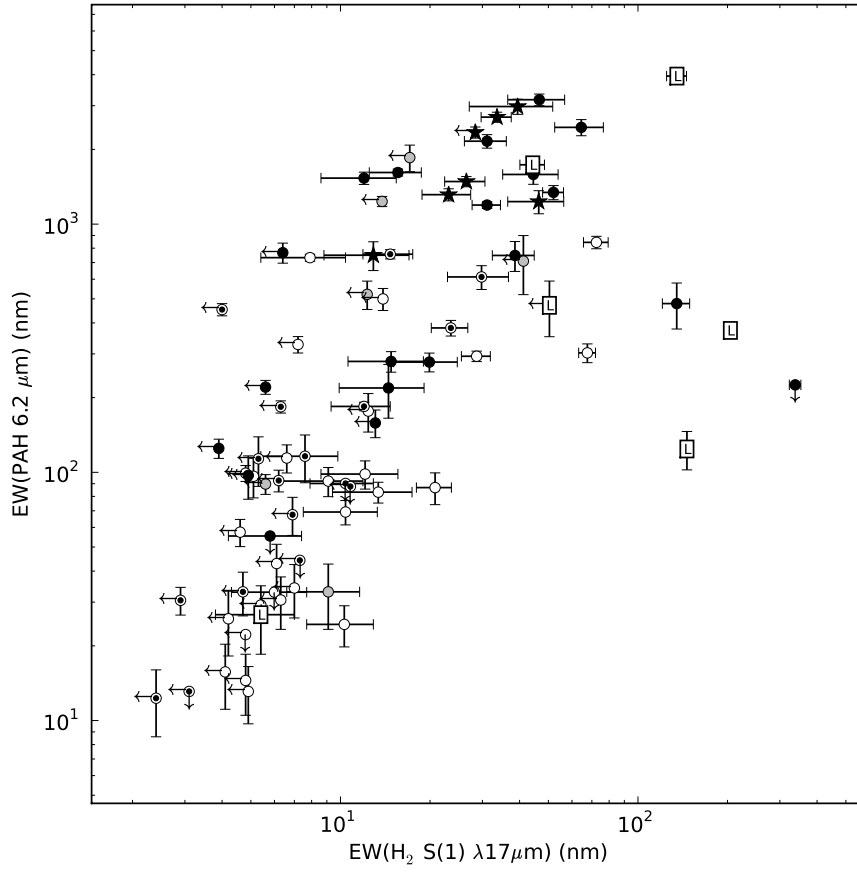


Fig. 10.— $6.2 \mu\text{m}$ PAH EW vs. $\text{H}_2 \text{ S}(1) 17\mu\text{m}$ EW. Open circles are S1, S1.5, and S1n, gray-filled circles are S1.8 and S1.9, filled circles are Sy 2, partially filled circles are “hidden Seyferts” (S1h and S1i), squares labeled L are LINERs, and filled stars are Starburst/HII galaxies. Limits are indicated by appropriately directed arrows.

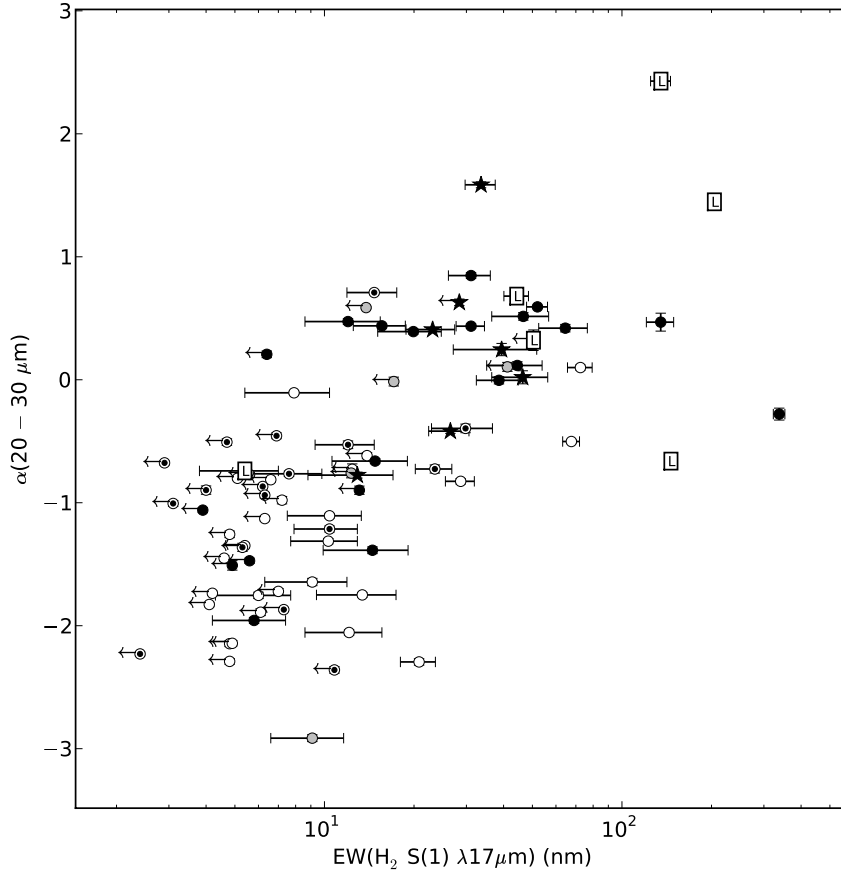


Fig. 11.— IRS 20-30 μm spectral index vs. H₂ S(1) 17 μm EW. We see a trend for sources with redder α_{20-30} to have larger molecular line EW. This is consistent with molecular hydrogen emission and a red SED both being signatures of star formation. Open circles are S1, S1.5, and S1n, gray-filled circles are S1.8 and S1.9, filled circles are Sy 2, partially filled circles are “hidden Seyferts” (S1h and S1i), squares labeled L are LINERs, and filled stars are Starburst/HII galaxies. Limits are indicated by appropriately directed arrows.

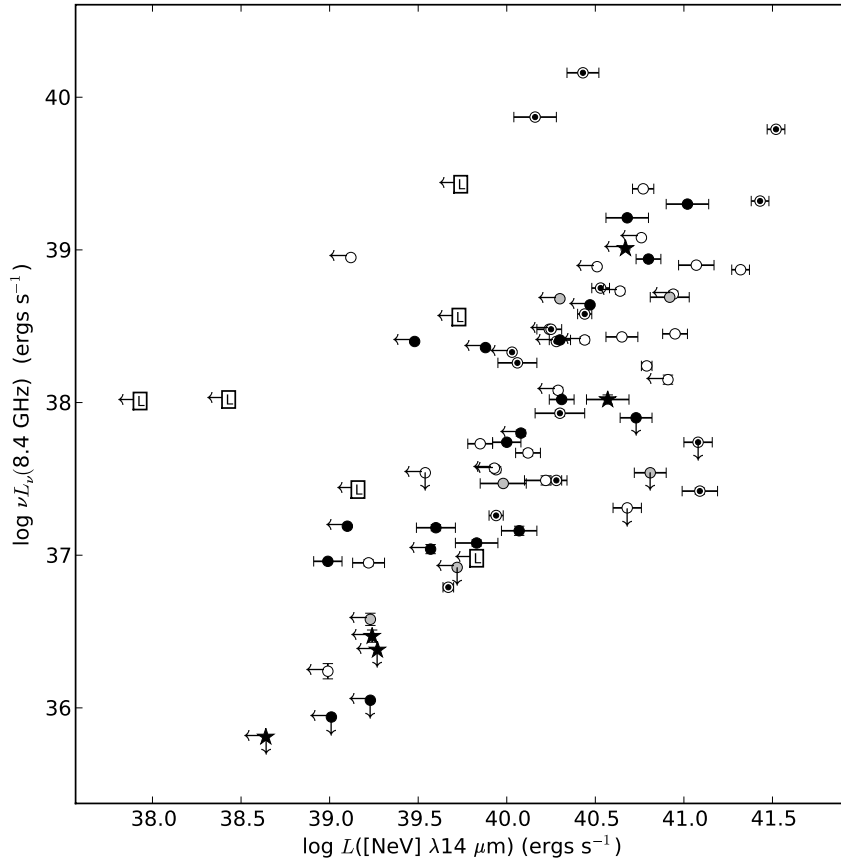


Fig. 12.— Luminosity of the [NeV] $14\mu\text{m}$ line vs. the luminosity of the 8 GHz radio continuum. Open circles are S1, S1.5, and S1n, gray-filled circles are S1.8 and S1.9, filled circles are Sy 2, partially filled circles are “hidden Seyferts” (S1h and S1i), squares labeled L are LINERs, and filled stars are Starburst/HII galaxies. Limits are indicated by appropriately directed arrows.

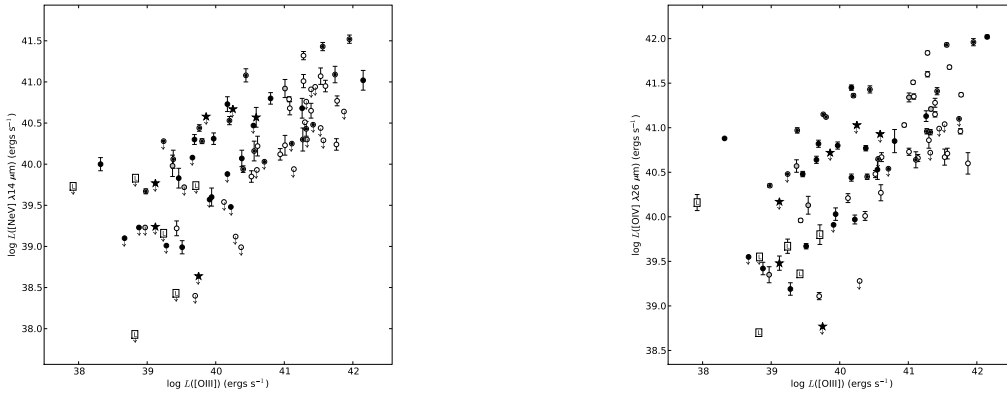


Fig. 13.— (Left). Luminosity of the [NeV] $14\mu\text{m}$ line vs. the luminosity of the [OIII] $\lambda 5007$ line. (Right). Luminosity of the [OIV] $26\mu\text{m}$ line vs. the luminosity of the [OIII] $\lambda 5007$ line. Open circles are S1, S1.5, and S1n, gray-filled circles are S1.8 and S1.9, filled circles are Sy 2, partially filled circles are “hidden Seyferts” (S1h and S1i), squares labeled L are LINERs, and filled stars are Starburst/HII galaxies. Limits are indicated by appropriately directed arrows.

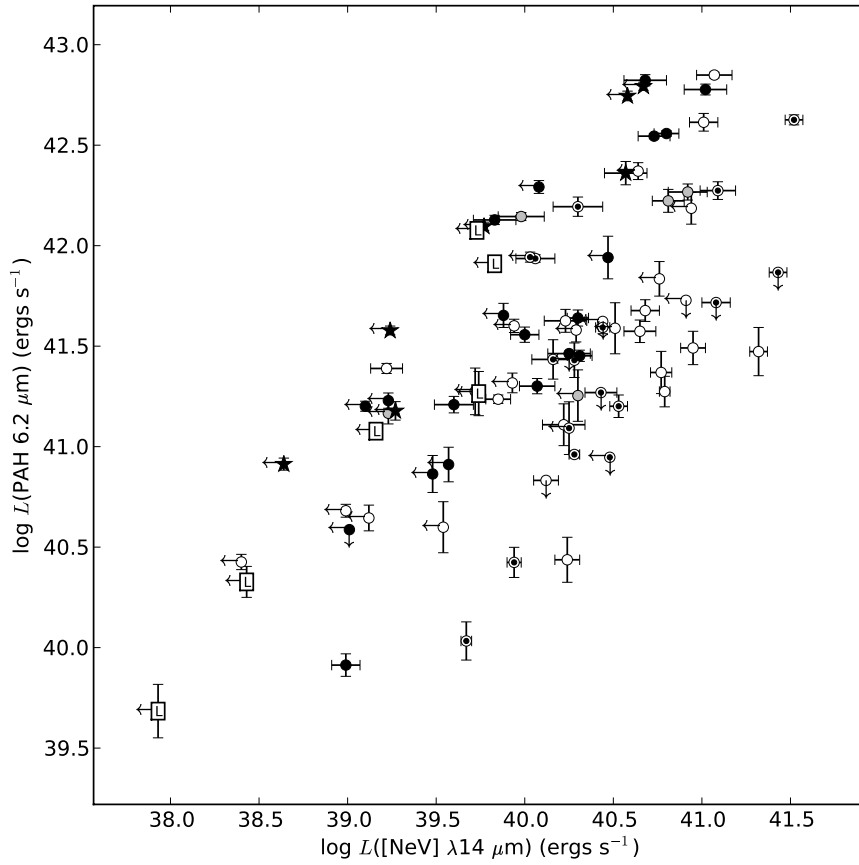


Fig. 14.— 6.2 μm PAH luminosity vs. [NeV] 14 μm luminosity. Open circles are S1, S1.5, and S1n, gray-filled circles are S1.8 and S1.9, filled circles are Sy 2, partially filled circles are “hidden Seyferts” (S1h and S1i), squares labeled L are LINERs, and filled stars are Starburst/HII galaxies. Limits are indicated by appropriately directed arrows.

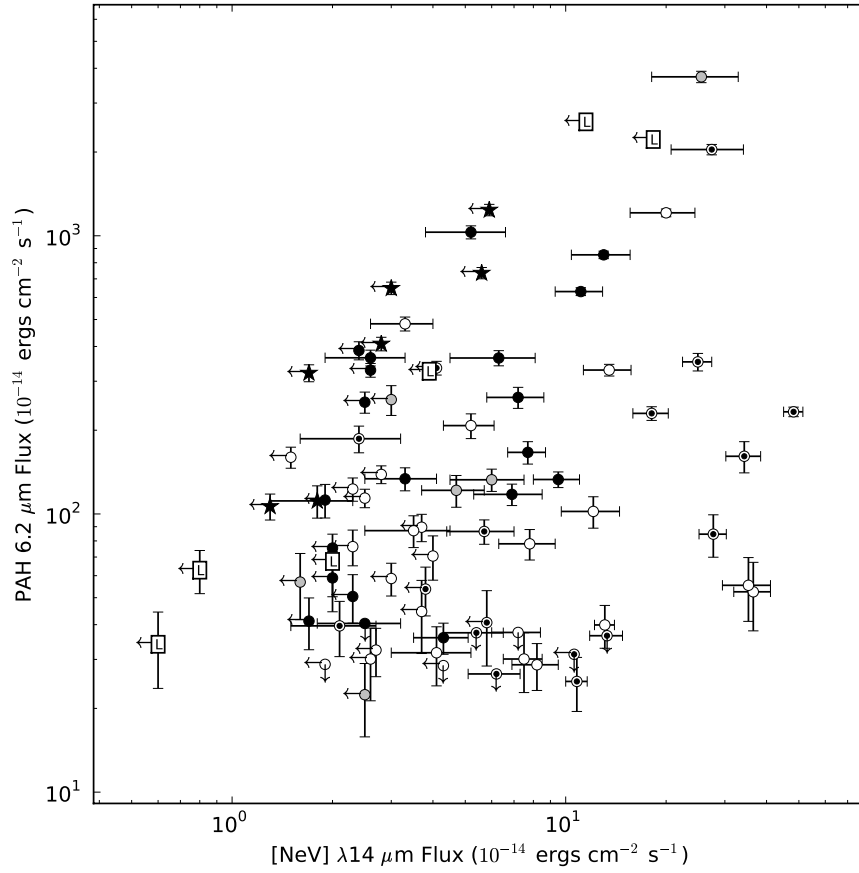


Fig. 15.— 6.2 μm PAH feature flux vs. [NeV] 14 μm line flux. This is an AGN vs Starburst relation. Open circles are S1, S1.5, and S1n, gray-filled circles are S1.8 and S1.9, filled circles are Sy 2, partially filled circles are “hidden Seyferts” (S1h and S1i), squares labeled L are LINERs, and filled stars are Starburst/HII galaxies. Limits are indicated by appropriately directed arrows.

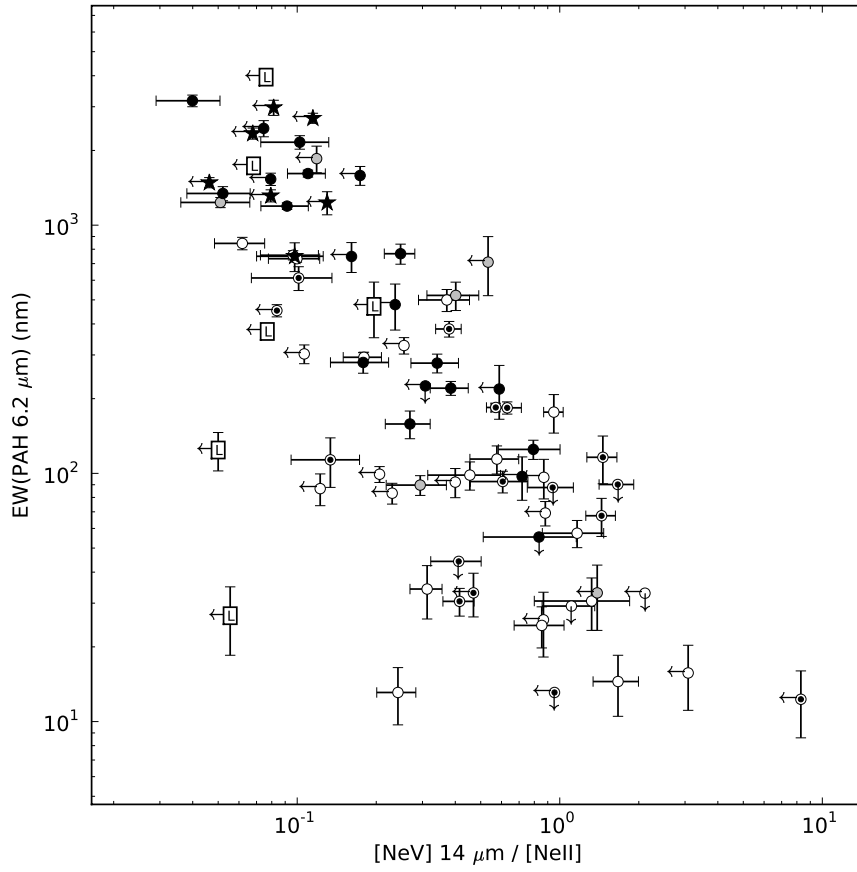


Fig. 16.— The ratio $[\text{NeV}]14\mu\text{m}/[\text{NeII}]12\mu\text{m}$ vs. $6.2\mu\text{m}$ PAH EW. Open circles are S1, S1.5, and S1n, gray-filled circles are S1.8 and S1.9, filled circles are Sy 2, partially filled circles are “hidden Seyferts” (S1h and S1i), squares labeled L are LINERs, and filled stars are Starburst/HII galaxies.

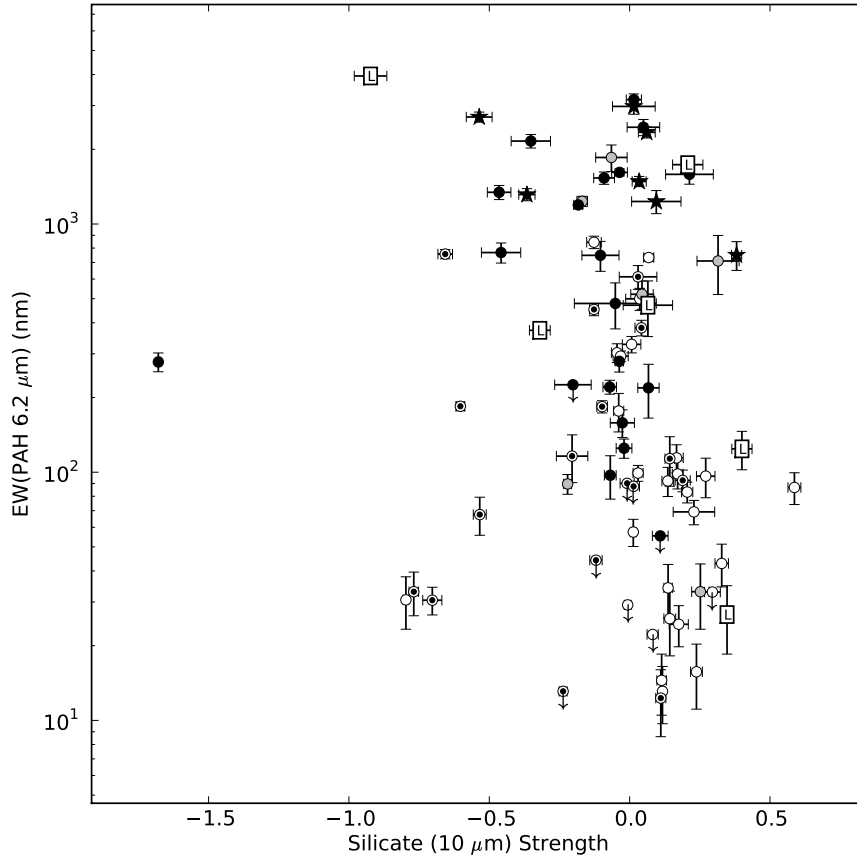


Fig. 17.— 6.2 μm PAH EQW vs. Sil 10 μm strength. For the Sil 10 strength, positive means emission. Open circles are S1, S1.5, and S1n, gray-filled circles are S1.8 and S1.9, filled circles are Sy 2, partially filled circles are “hidden Seyferts” (S1h and S1i), squares labeled L are LINERs, and filled stars are Starburst/HII galaxies. Limits are indicated by appropriately directed arrows.

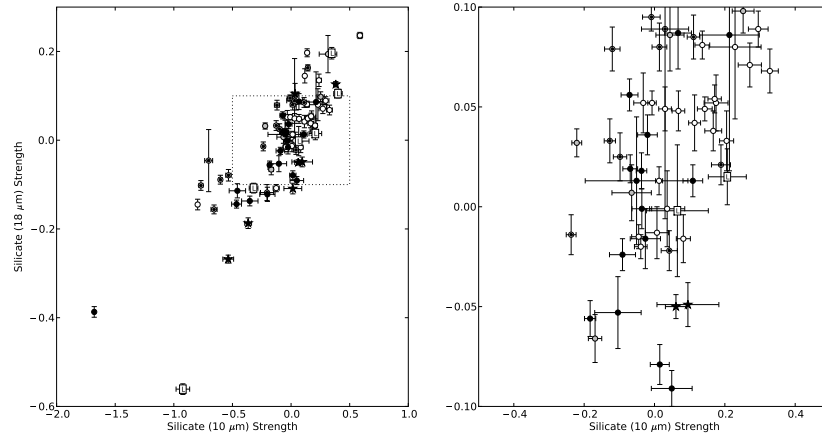


Fig. 18.— Sil 18 μm Strength vs. Sil 10 μm strength. For the Sil strength, positive means emission. (Left) All the points. Blow up of inset region is on the right. (Right) Blow up of region near Sil Strength of zero. Open circles are S1, S1.5, and S1n, gray-filled circles are S1.8 and S1.9, filled circles are Sy 2, partially filled circles are “hidden Seyferts” (S1h and S1i), squares labeled L are LINERs, and filled stars are Starburst/HII galaxies. Limits are indicated by appropriately directed arrows.

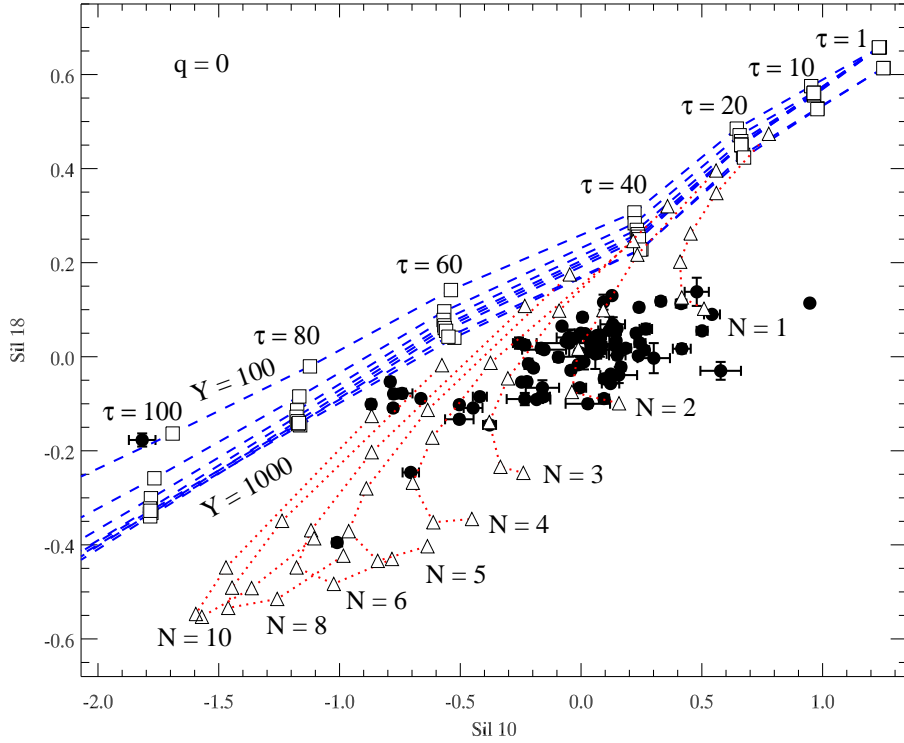


Fig. 19.— Sil 18 μm Strength vs. Sil 10 μm strength. For the Sil strength, positive means emission. Theoretical curves for spherical obscuration models (Sirocky et al. 2008) are shown. Dotted lines are clumpy models and dashed lines are smooth models. Model parameters are annotated: q is the power law index of the radial density distribution (here, flat); Y is the ratio of the outer radius to the inner radius of the obscuring region (spherical models, the inner radius is set by dust sublimation); τ refers to τ_V , the total opacity through the spherical shell (spherical models); and N refers to the average number of clumps along the sight-line (clumpy models). Spherical models range over $Y = 100, 200, 300, 400, 500, 600, 800, \& 1000$; $Y = 30$ for the clumpy models. The clumpy models are further distinguished by the (unlabeled) opacity through individual clumps: $\tau_V = 10, 20, 30, 40, 60, \& 80$, with lower opacities oriented to the upper right on this diagram.

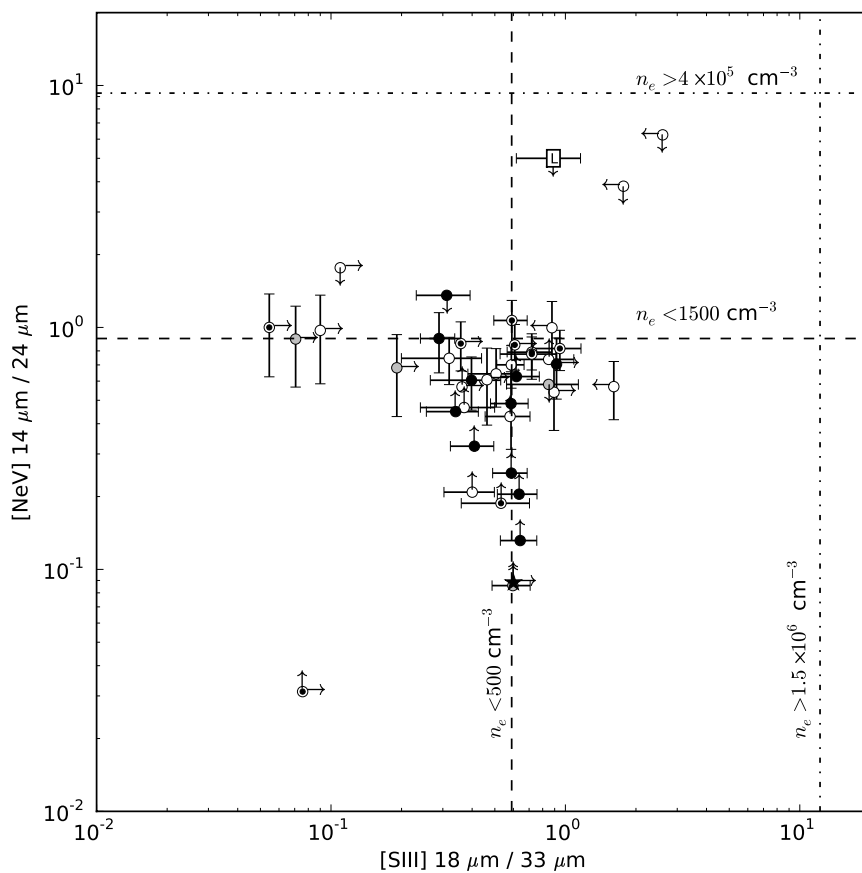


Fig. 20.— $[\text{NeV}] 14\mu\text{m}/24\mu\text{m}$ vs. $[\text{SIII}] 18\mu\text{m}/33\mu\text{m}$. Open circles are S1, S1.5, and S1n, gray-filled circles are S1.8 and S1.9, filled circles are Sy 2, partially filled circles are “hidden Seyferts” (S1h and S1i), squares labeled L are LINERs, and filled stars are Starburst/HII galaxies. Limits are indicated by appropriately directed arrows.

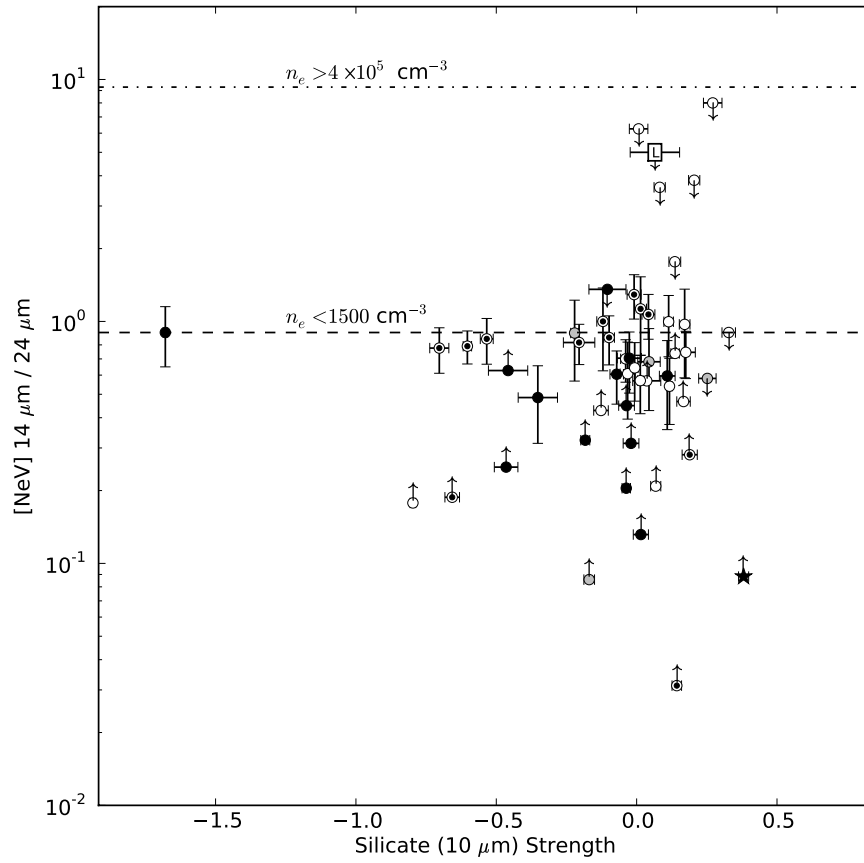


Fig. 21.— $[\text{NeV}] 14\mu\text{m}/24\mu\text{m}$ vs. Sil $10 \mu\text{m}$ strength. Open circles are S1, S1.5, and S1n, gray-filled circles are S1.8 and S1.9, filled circles are Sy 2, partially filled circles are “hidden Seyferts” (S1h and S1i), squares labeled L are LINERs, and filled stars are Starburst/HII galaxies. Limits are indicated by appropriately directed arrows.

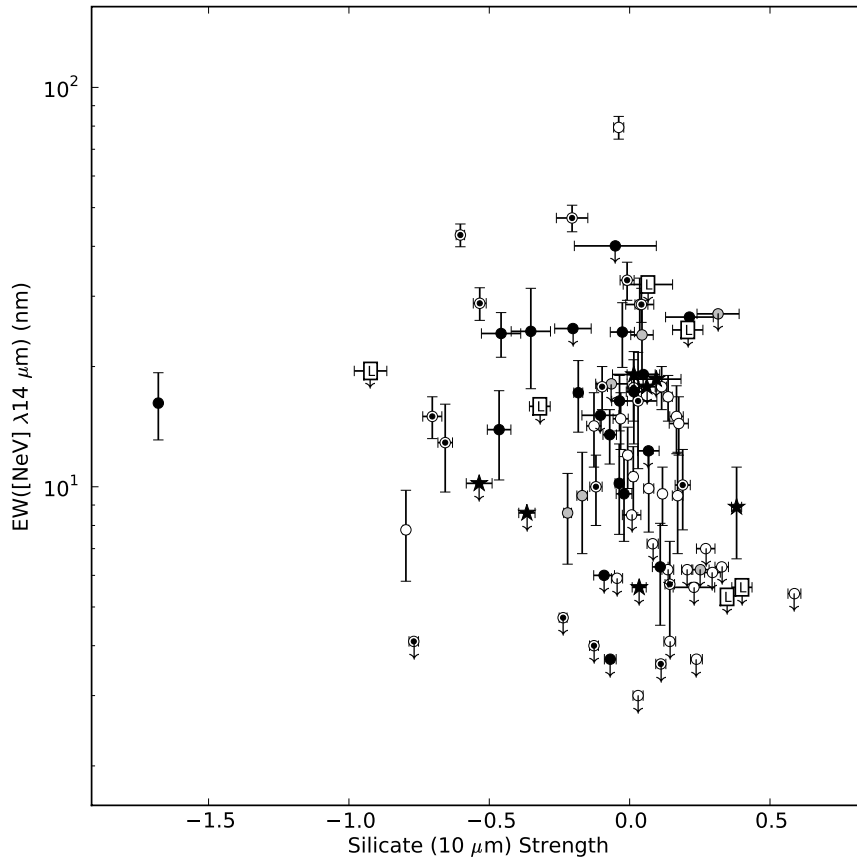


Fig. 22.— [NeV] $14\mu\text{m}$ EW vs. Sil $10\mu\text{m}$ strength. Open circles are S1, S1.5, and S1n, gray-filled circles are S1.8 and S1.9, filled circles are Sy 2, partially filled circles are “hidden Seyferts” (S1h and S1i), squares labeled L are LINERs, and filled stars are Starburst/HII galaxies. Limits are indicated by appropriately directed arrows.

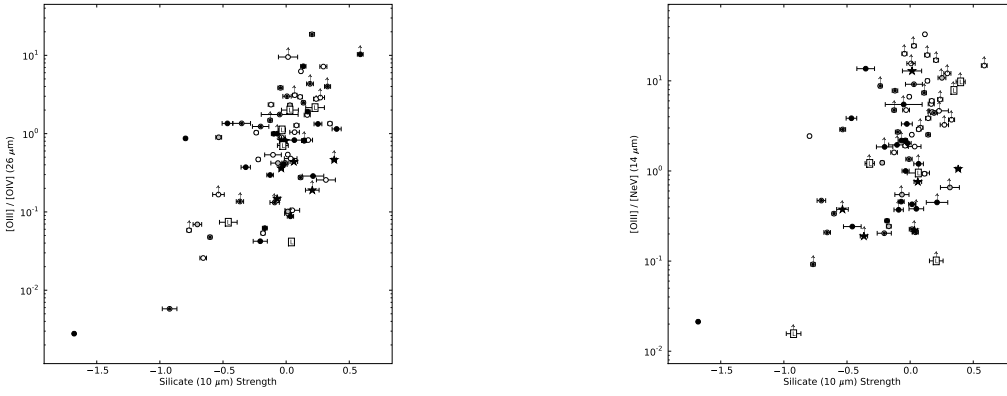


Fig. 23.— (Left) The ratio $[\text{OIII}]5007/[\text{OIV}]26\mu\text{m}$ vs. Sil $10\mu\text{m}$ strength. (Right) The ratio $[\text{OIII}]5007/[\text{NeV}]14\mu\text{m}$ vs. Sil $10\mu\text{m}$ strength. Open circles are S1, S1.5, and S1n, gray-filled circles are S1.8 and S1.9, filled circles are Sy 2, partially filled circles are “hidden Seyferts” (S1h and S1i), squares labeled L are LINERs, and filled stars are Starburst/HII galaxies. Limits are indicated by appropriately directed arrows.

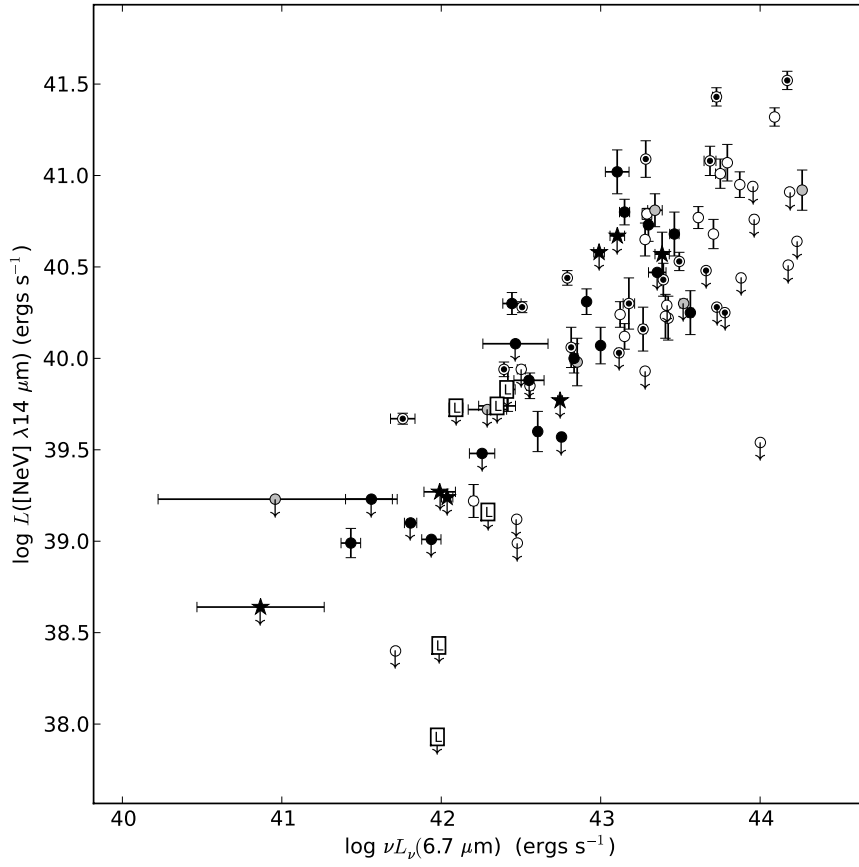


Fig. 24.— Luminosity of the [NeV] $14\mu\text{m}$ line vs. the luminosity of the continuum at $6.7\mu\text{m}$. Open circles are S1, S1.5, and S1n, gray-filled circles are S1.8 and S1.9, filled circles are Sy 2, partially filled circles are “hidden Seyferts” (S1h and S1i), squares labeled L are LINERs, and filled stars are Starburst/HII galaxies. Limits are indicated by appropriately directed arrows.